

Numerical CFD study on the frictional drag reduction using air lubrication

Jacob Bjørn Helmers Ottosen

Thermal Energy and Process Engineering, TEPE4-1005, 2022-06

Master's Thesis



Copyright © Aalborg University 2022

This project is written in Overleaf. The numerical simulations are performed using Open-FOAM. Results are analysed in ParaView, MATLAB and Spyder.



AAU Energy
Aalborg University
<http://www.aau.dk>

AALBORG UNIVERSITY

STUDENT REPORT

Title:

Numerical CFD study on the frictional drag reduction using air lubrication

Theme:

Master's Thesis

Project Period:

Spring Semester 2022

Project Group:

TEPE4-1005

Participant(s):

Jacob Bjørn Helmers Ottosen

Supervisor(s):

Jakob Hærvig
Kasper Gram Bilde

Page Numbers: 59

Date of Completion:

May 30, 2022

Abstract:

In this study a series of multi-phase Large Eddy Simulations with the Volume Of Fluid approach are made to analyse the use of air lubrication to reduce the drag on a ship by injecting air bubbles underneath the hull. The multi-phase simulations are initialised with a turbulent velocity profile obtained from simulations with a single-phase computational model, which is validated against theory, by comparing the turbulent boundary layer with the law of the wall. In the multi-phase simulations, the air volume fraction is varied from 14 - 50%. In the case with an air volume fraction of 14% a reduction in wall shear stress of 20 - 40% is seen. In the other cases with an air volume fraction from 27 - 50% a reduction of 40 - 60% in the wall shear stress is seen compared to the values using the single-phase model.

The content of this report is freely available, but publication (with reference) may only be pursued due to agreement with the author.

Summary

In this study a series of multi-phase Large Eddy Simulations with the Volume Of Fluid approach have been made to analyse the use of air lubrication to reduce the drag on a ship by injecting air bubbles underneath the hull. The Volume Of Fluid approach was chosen, as oppose to other less computationally demanding multi-phase methods, as it makes it possible to resolve the interface between the air and the water of each air bubble, which allows to analyse the dynamics of the air bubbles and the effect of those on the drag reduction. As the Volume of Fluid approach is computationally demanding, it is not possible to analyse the effect of air lubrication across an entire hull of a ship. Because of this a smaller domain of the size 50 x 180 x 50 mm was used with periodic boundary conditions with the surface of the hull represented as a flat plate. The velocity of the flow in the simulations was 5 m/s, and the simulated time was limited to 0.4 s, corresponding to a streamwise distance of 2 m.

A single-phase computational model was developed to obtain a turbulent velocity profile, which was used to initialise the flow in the multi-phase simulations. To ensure that the results of the single-phase simulation were independent of the mesh size, a grid convergence study was made. Furthermore the model was validated against theory, by comparing the turbulent boundary layer with the law of the wall.

Five multi-phase simulations were performed, where the air volume fraction was varied from 14 - 50% to analyse the effect of the air volume fraction on the drag reduction. At the start of the simulations, bubbles with a diameter $d = 2$ mm were inserted uniformly inside and outside of the turbulent boundary layer, to analyse the air bubble behaviour inside as well as outside of the turbulent boundary layer. Throughout the simulations two types of air bubble behaviour were seen; a coalescence of bubbles forming an air layer in the boundary layer near the wall and a splitting up of bubbles further away from the wall, where the latter was deemed to be caused by the vorticity in the flow.

The drag reduction with the use of air lubrication was analysed by comparing the wall shear stress for a case without air bubbles and the five cases with varying air volume fractions. A reduction in wall shear stress and thereby a reduction in drag was seen in the multi-phase simulations compared to the single-phase simulation. The wall shear stress decreased with 20 - 40% in case 1 with an air volume fraction of 14% compared to the wall shear stress in the single-phase simulation. For the other cases with air volume fractions of 27 - 50% the reduction in wall shear stress fluctuated from 40 - 60%. Analysing the structure of the air in the simulations it was found that the regime of highest achievable drag reduction with air lubrication, Air Layer Drag Reduction, was not obtained in the simulations.

Nomenclature

Symbols		Units
α	Water volume fraction	-
Δ	Minimum eddy length	m
δ	Turbulent boundary layer thickness	m
\dot{V}	Volume flow	m ³ /s
ν	Kinematic viscosity	m ² /s
ω	Vorticity	1/s
ρ	Density	kg/m ³
τ_w	Wall shear stress	Pa
φ	Air volume fraction	-
B	Experimental constant	-
cf	Skin friction coefficient	-
d	Diameter	mm
F	Force	N
g	Gravity	m/s ²
k	Von Kármán constant	-
L	Length	m
P	Pressure	Pa
q	Gas injection rate per unit span	m ² /s

R	Reynolds stress	Pa
Re	Reynolds number	-
t	Time	s
u	Velocity	m/s
u^+	Dimensionless velocity	-
u_τ	Friction velocity	m/s
V	Volume	m ³
y^+	Dimensionless distance	-

Subscripts

∞	Free stream
σ	Surface tension
φ	Air volume fraction
x	Downstream distance
c	Cell
crit	Critical
g	Gas
inj	Injection
k	Kinematic
l	Liquid
p	Periodic
rgH	Total hydrostatic
sim	Simulation

Abbreviations

ALDR	Air Layer Drag Reduction
AMR	Adaptive Mesh Refinement
BDR	Bubble Drag Reduction

CFD	Computational Fluid Dynamics
DNS	Direct Numerical Simulation
DR	Drag Reduction
EEDI	Energy Efficiency Design Index
LES	Large Eddy Simulation
MPLIC	Multicut Piecewise-Linear Interface Calculation
PCDR	Partial Cavity Drag Reduction
PLIC	Piecewise-Linear Interface Calculation
RANS	Reynolds Averaged Navier Stokes
SGS	Sub-grid scale
VOF	Volume Of Fluid
WALE	Wall Adapting Local Eddy-viscosity

Notations

\boldsymbol{x}	Vector
$\langle x \rangle$	Time averaging
\bar{x}	Space averaging
x'	Fluctuating component

Preface

The following report is a Master's Thesis on the 4th semester of M.Sc. in Thermal Energy and Process Engineering at the Department of Energy Technology at Aalborg University. The Thesis is written by Jacob Bjørn Helmers Ottosen in cooperation with Alfa Laval Aalborg A/S. The project was conducted in the period 1st of February 2022 to 30th of May 2022. In the Thesis the use of air lubrication to reduce the frictional drag on the hull of a ship is analysed numerically. The project is conducted under guidance of Jakob Hærvig and Kasper Gram Bilde.

Jacob Ottosen

Jacob Bjørn Helmers Ottosen
jottos17@student.aau.dk

Contents

Nomenclature	vii
1 Introduction	1
1.1 Air Lubrication	2
1.1.1 Mechanisms of air lubrication	4
1.2 Numerical approaches on air lubrication	5
2 Problem Statement	7
3 Theory	9
3.1 Boundary layer theory	9
3.2 Numerical Fluid Mechanics	11
3.2.1 Sub-grid scale model	11
3.2.2 Volume of Fluid	12
3.2.3 Governing Equations	12
3.3 Wall shear stress	13
4 Simulation Setup	15
4.1 Initialisation strategies	15
4.2 Boundary conditions	22
4.3 Meshing	23
4.3.1 Grid Convergence	24
4.4 Schemes	25
4.4.1 Interface Capturing	25
4.5 Time discretisation scheme	26
4.6 Simulations performed in this study	26
5 Validation of single-phase model	27
5.1 Parameters of interest	27
5.2 Comparison of the meshes	28

6 Results	31
6.1 Air bubble behaviour	31
6.2 Wall shear stress	35
7 Conclusion	41
7.1 Future work	43
References	45
A Equations	47
A.1 Equations used to determine the height of the cells closest to the wall	47
B Results	49
B.1 Air bubble behaviour	49
B.1.1 Case 1 ($\varphi = 14\%$)	49
B.1.2 Case 2 ($\varphi = 27\%$)	51
B.1.3 Case 3 ($\varphi = 37\%$)	53
B.1.4 Case 4 ($\varphi = 44\%$)	55
B.2 Vorticity	57

Chapter 1

Introduction

In the Paris agreement from 2015 it was agreed to keep the increase in global average temperature below 2°C compared to pre-industrial levels [UNFCCC (2015)]. In 2020 the EU and its members committed to a binding target of a net CO₂ emission reduction of at least 55% by 2030 compared to 1990 [EU (2020)].

The International Maritime Organization (IMO) adopted an initial strategy to reduce the green house gas emissions from ships by 2018 that would effectively reduce the CO₂ emissions from shipping by 40% in 2030 and more than 50% by 2050 compared to 2008 values.

Maritime transport has low CO₂ emissions compared to other methods of transportation as seen in Table 1.1. Even though maritime transport is the transportation method that emits the smallest mass of CO₂, it still accounts for 2.2% of the global CO₂ emissions, as 90% of the worlds goods transport is carried out with ships [Fenhann (2017)].

Table 1.1: CO₂ emissions with various transportation forms [Fenhann (2017)].

CO ₂ emissions by type of transportation	CO ₂ [g/km] per metric ton of freight.
Airplane (air cargo)	560
Modern lorry or truck	45
Modern train	18
Modern ship (Maersk Line, Triple E)	3

A rise in transport demand is expected which would consequently increase the CO₂ emissions from ships. In the fourth greenhouse gas study by IMO (2020) projections of CO₂ emissions of shipping from 2018-2050 are presented in various business-as-usual cases, in which it is assumed that no regulations are adopted to influence the emissions or the energy efficiency. It is projected that the CO₂ emis-

sions will be 0-50 % higher in 2050 compared to 2018.

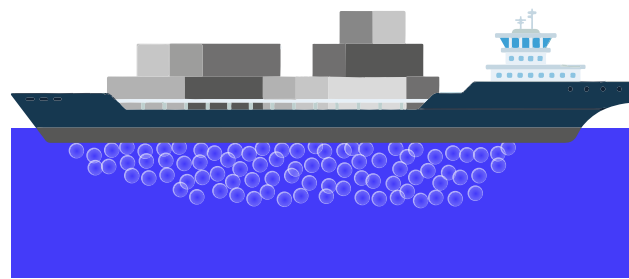
To reduce the emissions from ships, IMO has introduced an Energy Efficiency Design Index (EEDI) that all ships over 400 gross ton, which are newly built or ships that have undergone a major conversion, have to comply with. The EEDI is a measure of the ships energy efficiency in terms of gram CO₂ per capacity-mile. The EEDI implementation is divided into 4 phases, where the initial phase was started in 2013 and fully implemented by 2014. In this phase new ships had to meet the reference EEDI value for the given type of ship. Over the next three phases, the EEDI values will be reduced gradually, with each phase being a five year period. The requirements of reduction in CO₂ emissions in the different phases, compared to the base year 2013 are as follows:

- Phase one (2015): 10%
- Phase two (2020): 20%
- Phase three (2025): 25%

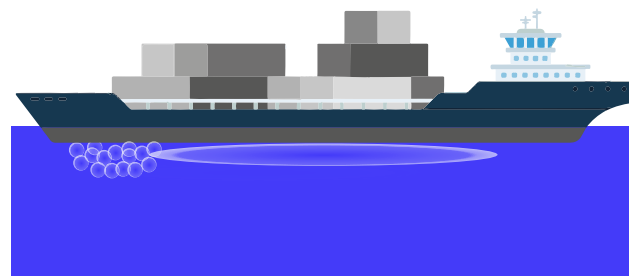
In order to meet the EEDI requirements shipowners have several options. These options include delaying ship-building, slow steaming, ship design, energy recovery and the use of alternative fuels [Fenhann (2017)]. In this project the focus will be on the use of air lubrication to reduce the frictional drag on the hull of ships, thereby reducing the fuel consumption and CO₂ emissions.

1.1 Air Lubrication

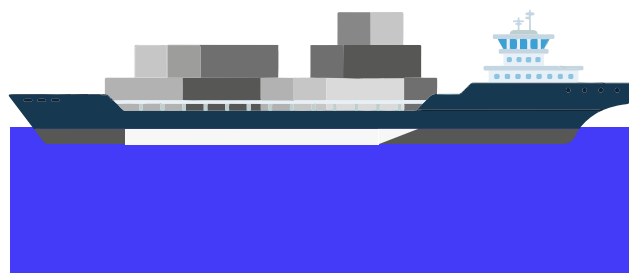
Air lubrication is the injection of air bubbles in the boundary-layer underneath the hull of a ship. This reduces the frictional drag on the ship, which reduces the fuel consumption of the ship. There are three general types of air lubrication, Bubble Drag Reduction (BDR), Air Layer Drag Reduction (ALDR) and Partial Cavity Drag Reduction (PCDR), which are illustrated in Figure 1.1.



(a) Bubble Drag Reduction (BDR)



(b) Air Layer Drag Reduction (ALDR)



(c) Partial Cavity Drag Reduction (PCDR)

Figure 1.1: Illustrations of the three general types of air lubrication.

BDR is the injection of small air bubbles underneath the hull of a ship. When the air flow is increased sufficiently the bubbles coalesce to form a continuous air layer known as ALDR. This results in a reduced skin friction drag, as a larger fraction of the wetted surface is in contact with the air [American Bureau of Shipping (2019)]. The drag reduction associated with BDR, ALDR and the transition between these two air lubrication methods is investigated experimentally in a study by Elbing et al. (2008), where it is found that the drag reduction (DR) is a function of the gas injection rate per unit span, as seen in Figure 1.2

The DR increases linearly in the BDR and transition regime, with a steeper slope in the transition region. The highest DR is achieved in the ALDR regime, where Elbing et al. (2008) observes close to 100% DR.

With PCDR an air layer is generated in a recess or cavity in the hull. This decreases the air injection rate required to maintain an air layer compared to ALDR, as the air leakage from the cavity is minimal when it has been filled with air [Mäkiharju, Perlin, and Ceccio (2012)].

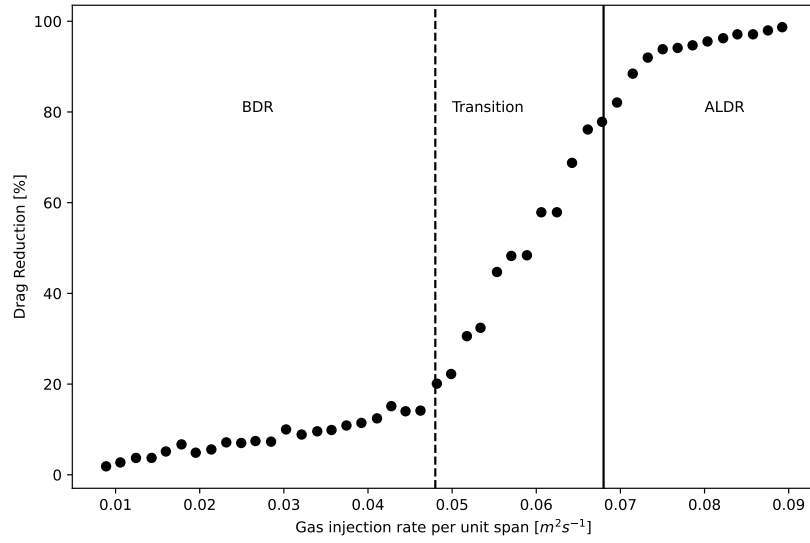


Figure 1.2: Drag reduction as function of the gas injection rate per unit span [Elbing et al. (2008)].

1.1.1 Mechanisms of air lubrication

In the literature it is generally agreed that the main mechanism for drag reduction with air lubrication is the reduction in mixture density and increase in mixture viscosity with the injection of bubbles. This reduces the Reynolds stress, R , shown in Equation 1.1, which results in a reduction of the skin friction.

$$R = \rho_{\phi} \overline{\mathbf{u}' \mathbf{u}'} \quad (1.1)$$

Herein ρ_{ϕ} is the effective density of the mixture and \mathbf{u}' is the velocity fluctuations.

Several studies including Legner (1984), Kato et al. (1999) and Jha, Bhatt, and Govardhan (2019) suggest that the interaction between the bubbles and the turbulence

in the buffer layer is the dominating mechanism in drag reduction with air lubrication. According to the study by Kato et al. (1999) the turbulent intensity in the buffer layer of the boundary layer increases as function of the air volume fraction, at low volume fractions, and decreases at higher volume fractions. The authors suspect that the turbulence of the bubble size could be suppressed by a cluster of micro-bubbles, due to the interference amongst the bubbles.

Skudarnov and Lin (2006) reported that the density ratio between the gas and liquid phase has a major influence on the drag reduction. The density ratio was varied in the range ($0.001 < \rho_{\text{ratio}} < 0.2$), by varying the density of the gas in the numerical simulations. At low gas injection rates, the density of the gas has little to no effect on the drag reduction, while at higher injection rates, the drag reduction increases gradually with decreasing gas density.

Similar experimental studies focusing on drag reduction are carried out by Kawamura et al. (2002), Takahashi et al. (2001) and Shen, Ceccio, and Perlin (2006), where all referred studies agree that the drag reduction is independent of the bubble size. However Merkle et al. (1989) concluded that the bubble size is an important parameter, as the trajectory of the bubbles and hence also the concentration of the bubbles and their location in the boundary layer is affected by their size. Furthermore, the buoyancy varies with the bubble diameter.

1.2 Numerical approaches on air lubrication

Several numerical approaches regarding the analyses of air lubrication have been reported in the literature. In a study by Wang et al. (2020) a two-way coupled Euler-Lagrange approach with bubbles treated as solid particles is used. The focus of the study was to analyse the burst frequency of eddies with and without the presence micro-bubbles. They concluded that the injection of micro-bubbles decreased the average burst frequency of the eddies, which was found to decrease the skin friction.

Skudarnov and Lin (2006) applied a single-phase model in which CO₂ gas micro-bubbles were introduced as a species mass source in the first layer of cells along a porous section of a flat plate. The species transport model is used to model the mixture density variation due the presence of micro-bubbles. Apart from their findings regarding the density ratio, they found that the single-phase model predicted the drag reduction in consistency with experimental data and more complex two-fluid model results.

The Volume Of Fluid (VOF) method is widely used in the literature to resolve the interface between gas bubbles in liquids. In a study by Tripathi, Sahu, and Govindarajan (2015), the VOF method is used to analyse the dynamics of an initially spherical bubble rising in liquid. By performing simulations with a range of ratios of gravitational, viscous and surface tension forces, Distinct regimes of bubble behaviour in terms of shape and motion were reported.

The VOF method is rarely used in the literature as a multi-phase model to analyse the effect of air lubrication, it is however a promising method to use, as the interface of the bubbles is resolved and the behaviour of gas bubbles is well represented using this method, as reported by Tripathi, Sahu, and Govindarajan (2015). For these reasons it is chosen to use the VOF method in this study to analyse the effect of air lubrication.

Chapter 2

Problem Statement

In this project a periodic section of the hull of a ship will be represented as a flat plate. A small computational domain with periodic boundary conditions is used, as it makes it possible to simulate the interface of air bubbles in the turbulent boundary layer and to analyse the frictional drag on the surface without needing excessive computational power.

The main focus of this study is to investigate the effect of air lubrication on the frictional drag on the hull of a ship. This includes analysing the influence of the air volume fraction in the boundary layer, and the interaction between the air bubbles and the turbulence in the boundary layer. This leads to the following problem statement:

How does air bubbles in the boundary layer affect the frictional drag in terms of wall shear stress on the hull of a ship?

- How does the air volume fraction in the boundary layer influence the frictional drag?
- Which interactions are seen between the air bubbles and the turbulent boundary layer, and how does these interactions influence the frictional drag?

Chapter 3

Theory

3.1 Boundary layer theory

Fluid flowing past a wall can be divided into two regions; the bulk of the flow region and the boundary layer region. Inside the bulk of the flow region, the viscosity can be neglected, whereas in the boundary layer, the viscosity must be taken into account. The flow in the boundary layer can either be laminar, transitional or turbulent. This depends on the Reynolds number, which is defined in Equation 3.1.

$$Re_x = \frac{u_\infty x}{\nu} \quad (3.1)$$

u_∞ is the free stream velocity, ν is the kinematic viscosity of the fluid, and x is the distance the fluid has moved in the streamwise direction along the plate from the leading edge.

In Figure 3.1 a two-dimensional sketch of the boundary layer beneath a flat plate is seen. As shown in the figure, the fluid approaches the plate as a plug flow. When the fluid reaches the plate, the flow is laminar. The boundary layer starts to build up, and after a transitional period it becomes turbulent. The transition to turbulent flow occurs at the critical Reynolds number. The critical Reynolds number for a flow along a flat plate is theoretically $Re_{x,crit} = 5 \cdot 10^5$. In reality, however, the value of $Re_{x,crit}$ depends on the amount of perturbation in the outer flow [Schlichting and Gersten (2016)].

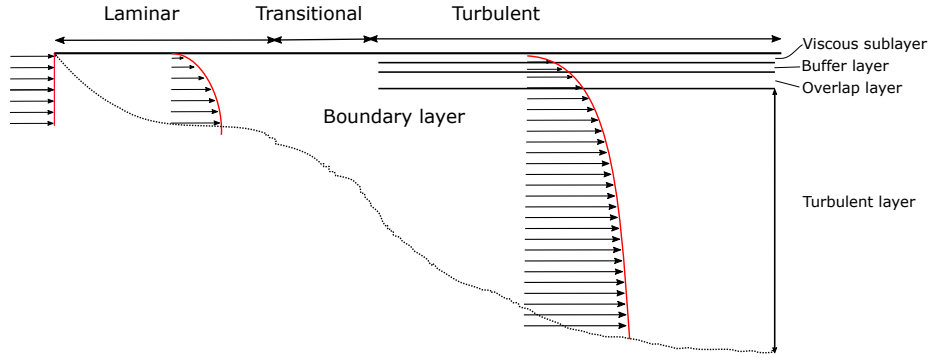


Figure 3.1: 2D Sketch of the developing boundary layer velocity profile on a flat plate.

The turbulent boundary layer thickness for turbulent flow across a flat plate $\delta(x)$, is determined using Equation 3.2 [Schlichting (1979)].

$$\delta(x) = 0.37 \frac{x}{Re_x^{1/5}} \quad (3.2)$$

The turbulent boundary layer is divided into 4 layers as illustrated in Figure 3.1 [Cengel, Cimbala, and Turner (2017)]. In the viscous sublayer the viscous effects are dominant. In the buffer layer and overlap layer, the turbulent effects on the flow increase gradually, with the flow still dominated by viscous effects. In the turbulent layer, also called the outer layer, the flow is dominated by the turbulent effects.

The velocity of the flow in the turbulent boundary layer is described with the dimensionless wall distance y^+ and velocity u^+ , which are described using Equation 3.3 and 3.4 respectively.

$$y^+ = \frac{yu_\tau}{\nu} \quad (3.3)$$

$$u^+ = \frac{u}{u_\tau} \quad (3.4)$$

u_τ is the frictional velocity which is described using Equation A.2, where τ_w is the wall shear stress.

$$u_\tau = \sqrt{\frac{\tau_w}{\rho}} \quad (3.5)$$

The relation between y^+ and u^+ in the different layers of the turbulent boundary layer is described by the law of the wall. In the viscous sublayer ($y^+ < 5$), the relation is described using Equation 3.6, in the overlap layer ($y^+ > 30$) the relation

is described using Equation 3.7 and in the buffer layer ($5 < y^+ < 30$) the relation is not well described.

$$u^+ = y^+ \quad (y^+ < 5) \quad (3.6)$$

$$u^+ = \frac{1}{k} \log(y^+) + B \quad (y^+ > 30) \quad (3.7)$$

In Equation 3.7 k is the Von Kármán constant which is 0.41. B is an experimentally determined constant with a value of 5.2.

3.2 Numerical Fluid Mechanics

The turbulence in the flow is predicted using a turbulence model. The three main categories of turbulence models are Reynolds Averaged Navier Stokes (RANS), Large Eddy Simulation (LES) and Direct Numerical Simulation (DNS). The RANS method is focused on the mean flow and the effect of the turbulence on the mean flow properties. With the LES method, the largest eddies are resolved, while the smallest eddies are modelled using a sub-grid scale model. With the DNS method all the turbulent fluctuations in the flow are resolved, which makes DNS the most costly method with regard to the computational demand, as resolving all sizes of turbulent eddies requires a high grid resolution and subsequently a smaller time step.

It is expected that the eddies in the flow affect the motion of the bubbles. This interaction between the eddies and the bubbles is not possible to analyse using the RANS method as the motion of the eddies is only included in the mean flow. The largest eddies in the flow contain the majority of the turbulent kinetic energy, which makes these worth resolving using the LES method. The smaller eddies which are resolved using the DNS method are not expected to affect the motion of the bubbles significantly as they dissipate into heat. It is therefore chosen to use the LES method as the turbulence model in this project.

3.2.1 Sub-grid scale model

With the LES method the eddies larger than a specified minimum eddy length are resolved. The eddies smaller than this length are not resolved and the interaction between these unresolved eddies and the larger resolved eddies is described using a sub-grid scale (SGS) model [Versteeg and Malalasekera (2007)]. The minimum eddy length used in this study is the cube root volume of the cells as seen in Equation 3.8.

$$\Delta = V_c^{1/3} \quad (3.8)$$

The SGS model used in this project is the Wall Adapting Local Eddy-viscosity (WALE) model by Nicoud and Ducros (1999). This SGS model has a number of advantages compared to the classical Smagorinsky model. The model detects all of the turbulent structures relevant for the kinetic energy dissipation. Neither a damping function or dynamic adjustment are needed to compute wall bounded flows, as the eddy-viscosity naturally goes to zero in the vicinity of a wall. Furthermore the model enables to reproduce the transition from laminar to turbulent flows, as the model produces zero eddy viscosity in case of pure shear.

3.2.2 Volume of Fluid

The multi-phase model chosen in this project is the Volume Of Fluid (VOF) model. This particular model is chosen as it is desired to resolve the interface between the air bubbles and the surrounding water. With the VOF method two or more immiscible fluids are modelled using one shared set of momentum equations and tracking the volume fraction of the fluids in the domain [Ansys and Inc (2009)]. The total volume fraction in each cell sum to 1, such that each cell is either fully occupied by water when $\alpha = 1$, fully occupied by air when $\alpha = 0$, or is a mixture of water and air $0 < \alpha < 1$. Based on the value of α the Navier Stokes equations are either solved using the properties of air or water, or mixture properties in the cells at the interface between the air bubbles and the water.

3.2.3 Governing Equations

The governing equations in CFD are the Navier Stokes equations. They describe the motion of a Newtonian fluid, which is defined by a set of two partial differential equations, a continuity equation and a momentum equation.

The continuity and momentum equations for Newtonian incompressible isothermal single-phase flow is presented in Equations 3.9 and 3.10. The continuity equation and momentum equation specify the conservation of mass and momentum in each cell in the discretised computational domain.

$$\nabla \cdot \mathbf{u} = 0 \quad (3.9)$$

$$\frac{\partial \mathbf{u}}{\partial t} + \nabla \cdot (\mathbf{u}\mathbf{u}) = -\nabla p_k + \nu \nabla^2 \cdot \mathbf{u} \quad (3.10)$$

Equation 3.10 also describes the conservation of mass for two Newtonian incompressible, isothermal immiscible fluids. The momentum equation, however, is

slightly different as seen in Equation 3.11, as a shared momentum equations is used for the two phases.

$$\frac{\partial(\rho_\alpha \mathbf{u})}{\partial t} + \nabla \cdot (\rho_\alpha \mathbf{u} \mathbf{u}) = -\nabla p_{\text{rgh}} + \mu_\alpha \nabla^2 \cdot \mathbf{u} + \rho_\alpha \mathbf{g} + \mathbf{F}_\sigma \quad (3.11)$$

\mathbf{F}_σ is the surface tension and the variables ρ_α and μ_α are the effective density and dynamic viscosity based on the volume fraction α in each cell, which are described using Equation 3.12 and 3.13 respectively, where the subscripts l and g represents liquid and gas.

$$\rho_\alpha = \alpha \rho_l + (1 - \alpha) \rho_g \quad (3.12)$$

$$\mu_\alpha = \alpha \mu_l + (1 - \alpha) \mu_g \quad (3.13)$$

Equation 3.14 is used for the interface to describe the conservation of mixture properties in the cells.

$$\frac{\partial \alpha}{\partial t} + \nabla \cdot (\alpha \mathbf{u}) = 0 \quad (3.14)$$

3.3 Wall shear stress

The wall shear stress on a flat plate is described by Equation 3.15. Generally the dynamic density ratio between air and water is $\mu_g/\mu_l \approx 10$. This implies that the wall shear stress is 10 times lower for air compared to water, if the velocity gradient is the same for the two fluids.

$$\tau_w = \mu_\varphi \frac{\partial \mathbf{u}}{\partial y} \quad (3.15)$$

The skin friction coefficient is described using Equation 3.16. Even though the wall shear stress is 10 times lower with air than water, the density ratio between air and water is $\rho_g/\rho_l \approx 0.001$. This makes the skin friction 100 times lower for air compared to water. Because of this, injecting air into the boundary layer underneath the hull of a ship should decrease the frictional drag.

$$c_f = \frac{\tau_w}{\frac{1}{2} \rho_\infty u_\infty^2} \quad (3.16)$$

Chapter 4

Simulation Setup

4.1 Initialisation strategies

If the aim is to analyse the effect of the air lubrication from the injection point and downstream, the flow could be initialised with a plug flow, which is illustrated in Figure 4.1. This means that the flow has a uniform constant velocity pointing in the streamwise flow direction. When the bubbles are injected into a plug flow, the boundary layer develops with the bubbles in the flow. This way it is possible to analyse the interaction between the boundary layer and the bubbles throughout the development of the turbulent boundary layer. A possible issue arising when injecting the bubbles in a plug flow, is that as the flow develops, the motion of the bubbles is primarily influenced by the mean flow velocity and the buoyancy and as a result the bubbles could rise to the surface of the hull prior to the turbulence in the flow influencing their motion. If all bubbles are rising to the surface, an air layer could be formed. This would increase the drag reduction and thereby the drag reduction could be overestimated. A way to overcome this issue is to accelerate the transition to a turbulent flow by introducing disturbances in the initial flow field.

If the aim is to analyse the effect of the air lubrication at a specific downstream location from the injection point, the flow could instead be initialised with the expected turbulent velocity profile, illustrated in Figure 4.1, at that specific location. This velocity profile could be a theoretical turbulent velocity profile obtained using boundary layer theory, or it could be obtained using a single-phase simulation, in which the flow develops along the primary flow direction.

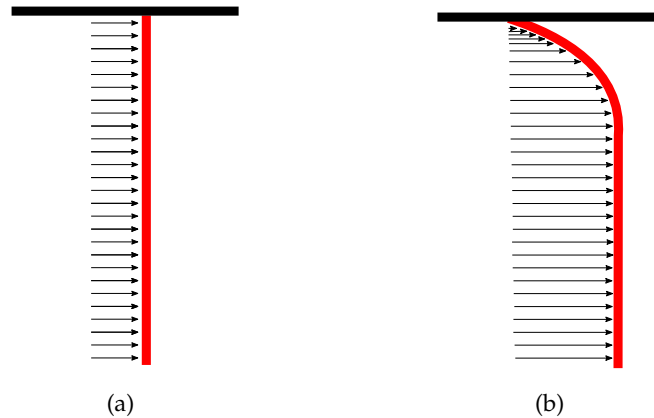


Figure 4.1: Illustrations of a plug flow velocity profile (a) and a turbulent velocity profile (b).

Based on the above mentioned simulation methods, it is chosen to inject the bubbles into a turbulent flow using a flow profile from a single-phase simulation. This method is chosen to avoid the possible overestimation of the drag reduction from bubbles rising to the surface of the hull when initialising with a plug flow as mentioned earlier. Another reason for initialising the multi-phase simulation with a turbulent developed velocity profile, as opposed to a plug flow with introduced disturbances in the velocity field in a part of the domain, is that this makes it possible to validate the computational model with single-phase simulations in a grid convergence study prior to performing the multi-phase simulations with injected bubbles.

The flow field is initialised with a constant velocity of 5 m/s. This velocity is chosen as it is assumed to represent the cruising or slow steaming velocity of a ship. A higher velocity could be used, but this would increase the computational cost of the simulations as the size of the cells in the near wall mesh would increase and the time step would decrease.

Analysing the effect of air lubrication on the frictional drag on the hull of a ship using CFD is challenging especially due to the differences in length scales. A ship is several 100 metres long, while the bubbles have a diameter of a few millimetres. The VOF modelling approach where the interface between the air bubbles and the water is resolved, requires at least 8 cells per bubble to resolve the interface. This results in an enormous number of computational cells, which implies an excessive amount of computational power. As an example if the aim is to track the motion of bubbles with a diameter $d = 2$ mm in a section of $200 \times 20 \times 1$ m underneath the hull of a ship, it would be required to discretise the section into 400 billion cells. The amount of required cells could be reduced using Adaptive Mesh Refinement

(AMR), where the mesh is refined at the interface between the bubbles and the water which allows for a coarser mesh in regions without bubbles. Even with the aid of AMR, the required amount of cells is still enormous.

A way to reduce the required amount of cells and thereby the computational cost significantly is to use periodic boundary conditions, which allows to analyse the effect of air lubrication along the hull of a ship using a smaller computational domain.

With periodic boundary conditions the flow at a pair of boundary patches is coupled. If periodic boundary conditions are specified between the inlet and outlet patches of the domain, the flow is essentially recycled throughout the domain. This allows the use of a smaller domain, rather than having a large domain in which the flow only passes through once. In Figure 4.2 the concept of using periodic boundary conditions on a section underneath the hull of a ship is illustrated.

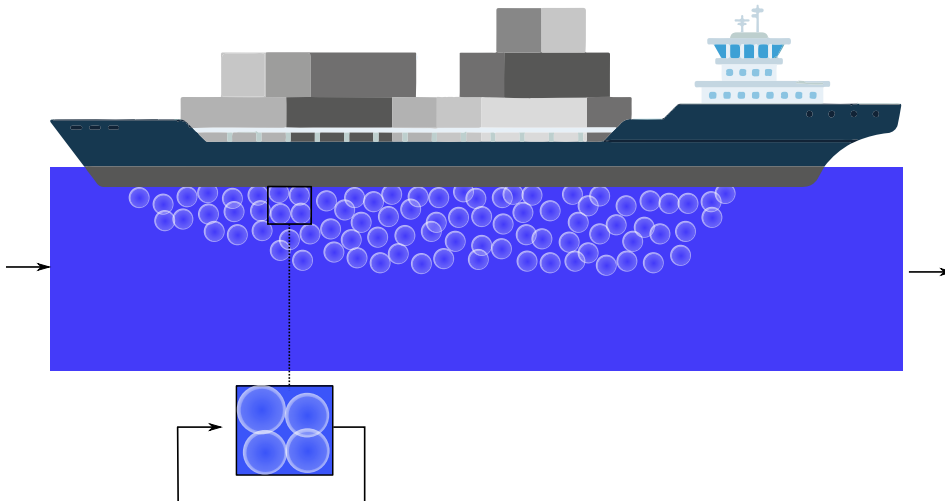


Figure 4.2: 2D illustration of the use of periodic boundary conditions on a small section within a large domain.

It is chosen to limit the simulation time based on a the fluid moving a distance of 2 m from the leading edge of the hull in both the single-phase and multi-phase simulations yielding a simulated time of $t_{\text{sim}} = 0.4$ s.

The size of the computational domain is chosen based on the estimated turbulent boundary layer thickness for turbulent flow across a flat plate $\delta(x)$, which is determined using Equation 3.2. As the flow obtained using the single-phase simulations will be used to initialise the multi-phase simulations, the single-phase and

multi-phase domains have the same dimensions in the x and z directions. In the y direction, which is the wall normal direction, the length of the multi-phase domain is doubled compared to the single-phase domain, as the growth of the turbulent boundary layer thickness is assumed to follow Equation 3.2. In Table 4.1 the dimensions of the domains are listed, and in Figure 4.3 an illustration of the domains and their relative dimensions are shown.

Table 4.1: Dimensions of the single-phase and multi-phase domains.

Simulation	L_x, L_z	L_y	$\delta(x)$
Single-phase	0.05	0.09	0.03
Multi-phase	0.05	0.18	0.05

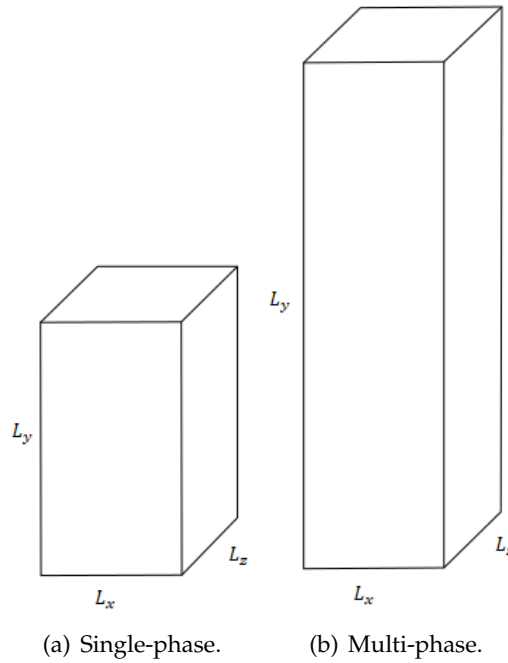


Figure 4.3: Illustration of the two domains.

To speed up the transition of the flow from laminar to turbulent, disturbances are added to the flow in the near wall region ($0 < y^+ < 10$). This is done by initialising the velocity in 4 cross-sectional regions with a wall normal component, such that the absolute flow is directed towards the wall with an angle of 30° , as oppose to the rest of the domain, where the flow is initialised with a velocity of 5 m/s in the streamwise flow direction. This is shown in Figure 4.4, where the data axis is in mm, to show the size and location of the regions initialised.

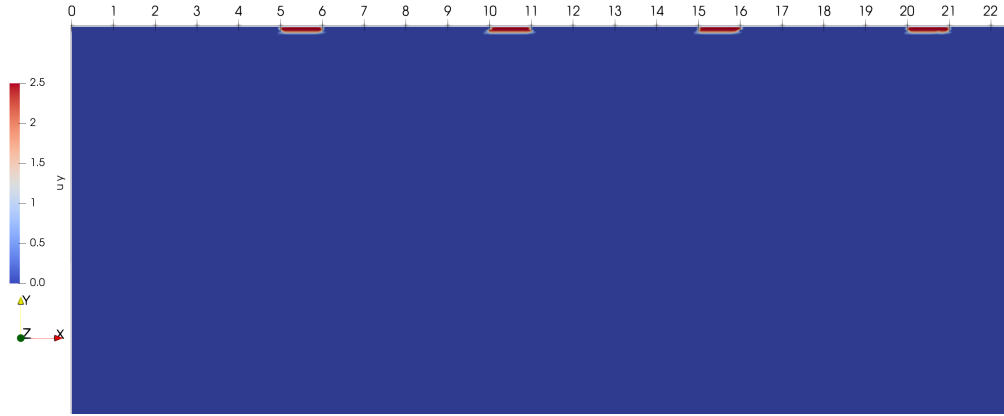


Figure 4.4: Illustration of the initial disturbance added to the flow in the near wall region. Visualised by the added wall normal component to the velocity vector u_y .

In the multi-phase simulations a range of air volume fractions will be analysed. The air volume fraction ϕ is specified using Equation 4.1, where V_{bubbles} is the total volume of the bubbles and $V_{\delta(2)}$ is the volume inside the theoretical length of the turbulent boundary layer after 2 m, which is the area of interest.

$$\phi = \frac{V_{\text{bubbles}}}{V_{\delta(2)}} \quad (4.1)$$

The range of air volume fractions to be analysed is chosen based on Figure 1.2 presented in Section 1.1. The figure shows the drag reduction at the different regimes of air lubrication based on the gas injection rate per unit span. To analyse if a similar relation between the gas injection rate and the drag reduction is seen from the multi-phase simulations, it is chosen to base the air volume fractions on the gas injection rate per unit span. To analyse the drag reduction in the different regimes, two simulations with an air volume fraction in the BDR regime, two simulations in the transition regime and one simulation in the ALDR regime are performed.

To determine the air volume fractions, firstly the number of bubbles as function of the volume fraction is obtained using Equation 4.2.

$$n_{\text{Bubbles}}(\phi) = \phi \cdot \frac{V_{\delta(2)}}{V_{\text{bubble}}} \quad (4.2)$$

The total volume of the air bubbles is determined using Equation 4.3.

$$V_{\text{bubbles}} = V_{\text{bubble}} \cdot n_{\text{bubbles}} \quad (4.3)$$

The volume flow of the bubbles is determined using Equation 4.4, where t_p is the time it takes for the fluid to travel a distance of 50 mm, which is the length of the domain in the streamwise direction.

$$\dot{V}_{\text{bubbles}} = \frac{V_{\text{bubbles}}}{t_p} \quad (4.4)$$

Lastly the gas injection rate per unit span q is determined using Equation 4.5, where L_z is the cross-sectional length of the domain.

$$q = \frac{\dot{V}_{\text{bubbles}}}{L_z} \quad (4.5)$$

Using these equations five cases of air volume fractions are chosen. An overview of these cases is presented in Table 4.2.

Table 4.2

Case	ϕ [%]	q [m ² /s]	Region of Air Lubrication
1	14	0.021	BDR
2	27	0.040	BDR
3	37	0.055	Transition
4	44	0.066	ALDR
5	50	0.075	ALDR

The bubbles are injected randomly in a volume of the size $V_{\text{inj}} = L_x \cdot L_z \cdot 2 \cdot \delta(2)$ as shown in Figure 4.5 to include the effect of the turbulence inside the boundary layer as well as the free stream flow on the motion of the bubbles.

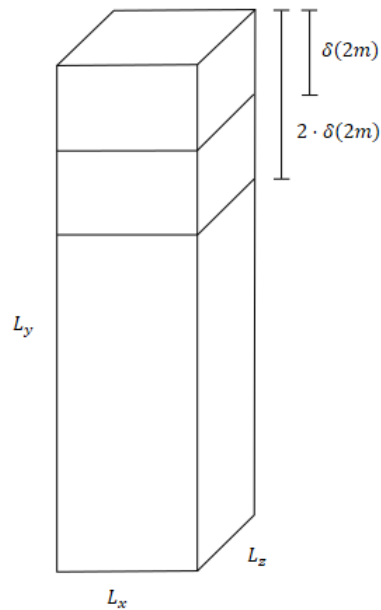


Figure 4.5: Illustration of the volume of bubble injection.

To inject the bubbles randomly within V_{inj} it was initially decided to obtain the locations of the bubbles based on a random set of coordinates for each bubble within this volume. This process however became challenging when each bubble should be placed in a unique location, such that none of the bubbles were placed at the same location, nor overlapped each other.

Instead of inserting the bubbles randomly, they were instead inserted in a more structured way, based on a uniform grid within this volume with the number of nodes corresponding to the amount of bubbles to be injected in each case. The number of nodes in the grid does however not completely match the number of bubbles as the grid is uniform. Because of this, the specified number of bubbles are randomly selected on the grid, as illustrated in Figure 4.6, where the black points are the selected coordinates for the locations to inject the bubbles. The Figure shows the grid and selected coordinates for case 1 with an air volume fraction of 14%, but the same procedure is used for the other cases.

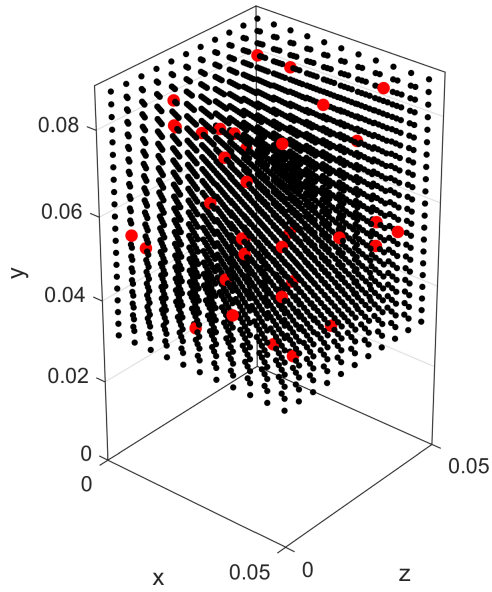


Figure 4.6: Illustration of the injection of bubbles based on a structured grid.

4.2 Boundary conditions

The boundary conditions used for the single-phase and multi-phase simulations are presented in Table 4.3. Wall is the solid flat plate representing the surface of a hull and Free stream is the boundary patch at the bottom of the domain parallel with the plate. For the velocity the no-slip boundary condition is applied to the wall while a fixed value of 5 m/s is applied to the free stream boundary patch, to conserve the momentum of flow in the simulations. For the pressure p and p_{rgh} , the turbulent viscosity ν_t and the volume fraction of water α_w the Neumann boundary condition is applied to the wall and free stream boundaries. For the wall shear stress τ_w the calculated boundary condition is applied to the wall and free stream boundaries, which means that τ_w is calculated at these boundaries. However as the free stream boundary is not a solid surface, τ_w remains 0 throughout the simulations at this boundary. Periodic boundary conditions are applied to the other boundaries, with the cyclic boundary condition. This implies that the flow is recycled in the simulation in the x and z direction.

Table 4.3: Boundary conditions in the single-phase and multi-phase simulations

Variable	Wall	Free stream	Other
Single-phase			
\mathbf{u}	no-slip	fixed value	cyclic
p	Neumann	Neumann	cyclic
ν_t	Neumann	Neumann	cyclic
τ_w	calculated	calculated	cyclic
Multi-phase			
\mathbf{u}	no-slip	fixed value	cyclic
p_{rgh}	Neumann	Neumann	cyclic
ν_t	Neumann	Neumann	cyclic
τ_w	calculated	calculated	cyclic
α_w	Neumann	Neumann	cyclic

4.3 Meshing

The near wall mesh needs to be sufficiently fine in order to resolve the developing turbulent boundary layer. To resolve the turbulence in the near wall region, the layer of cells closest to the wall needs to be placed inside the viscous sub-layer ($y^+ < 5$), preferably at $y^+ = 1$. The height of these cells is chosen based on the approximate height corresponding to $y^+ = 1$. Using the equations in Appendix A, this height is approximately $1.5 \cdot 10^{-5}$ m.

One way to achieve a cell height of the cells closest to the wall corresponding to $y^+ = 1$ without having an excessive amount of cells in the rest of the mesh is to grade the mesh in the direction towards the wall, while having a fixed cell length in the other directions. This, however, generates cells with increasing aspect ratios towards the wall. This method is not chosen, as having cells with high aspect ratios, could affect the representation of the interface of the air bubbles.

The aspect ratio can be reduced by dividing the near wall mesh into blocks, each with cells of the same size. This however imposes the issue of the faces of the cells not matching between the different blocks. A solution to this issue is to use face merging by specifying the patches between each block and merging them.

The domain is divided into 5 blocks, of which the first 4 blocks near the wall each contain a layer of 5 cells in the wall normal direction. The cells in the block closest to the wall have a length in the wall normal direction of 0.015 mm, satisfying $y^+ = 1$. In order to decrease the amount of cells, they have an aspect ratio of 4,

making them 0.045 mm in the other directions. Between each block, the wall normal length of the cells is doubled, while maintaining the same aspect ratio. This means that the dimensions of the cells are doubled in each directions between each block. A sketch of the relative difference in size of the cells in the different blocks is shown in Figure 4.7.

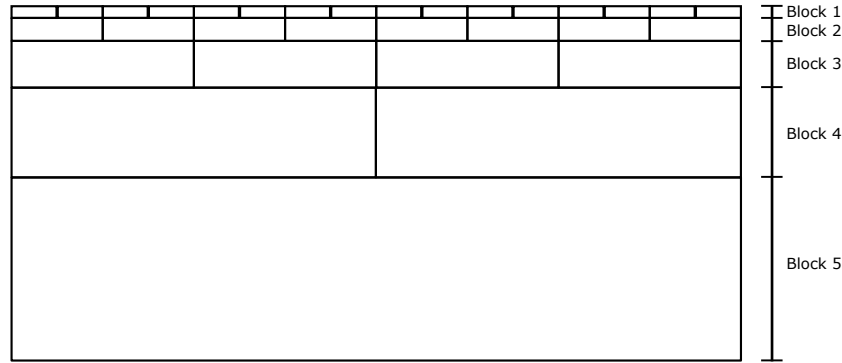


Figure 4.7: 2D Sketch of the relative difference in size of the cells in the different blocks.

4.3.1 Grid Convergence

To ensure that the results are independent of the mesh size, a grid convergence study is made. Time and spatial averaged velocity profiles are compared between a coarse, medium and a fine mesh.

In order to maintain $y^+ = 1$, the cells in Block 1 are unchanged throughout the meshes. In the other blocks, the length of the cells is doubled in the y -direction between the meshes, while maintaining the same dimensions in the x and z directions. A 2D sketch of the relative difference in size of the cells in the blocks of the meshes is shown in Figure 4.8. For simplicity only the first 3 blocks of each mesh are shown represented by one layer of cells.

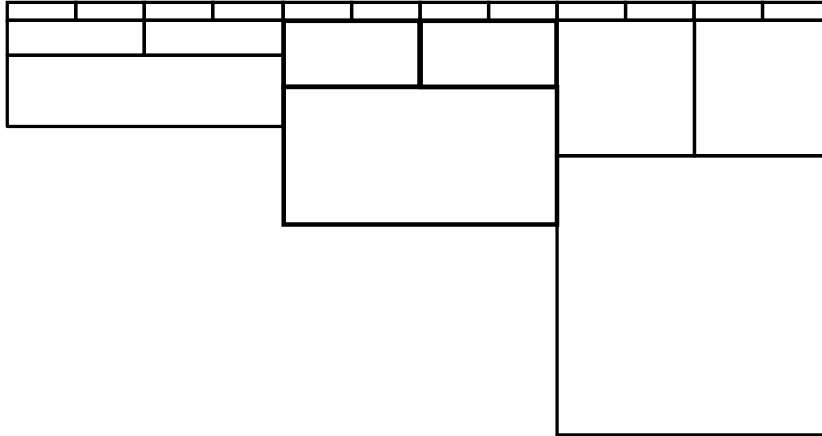


Figure 4.8: 2D sketch of the relative difference in size of the cells in the first 3 blocks of the meshes.

The amount of cells in the first 4 blocks remains the same in the different meshes, as the dimensions of the cells in the x and z direction, and the amount of cells in the y direction are unchanged between the meshes. Because of this, the amount of cells in the meshes change based on the number of cells in block 5. The amount of cells in the different meshes are shown in Table 4.4.

Table 4.4: Amount of cells in the different meshes.

Amount of cells	Coarse	Medium	Fine
Block 1	3,472,220	3,472,220	3,472,220
Block 2	868,056	868,056	868,056
Block 3	217,014	217,014	217,014
Block 4	54,253	54,253	54,253
Block 5	24,1428	493,707	1,003,690
Total amount of cells	4,852,973	5,105,251	5,615,234

4.4 Schemes

4.4.1 Interface Capturing

To capture the interface between air and water, the Multi Piecewise-Linear Interface Calculation (MPLIC) scheme is used. The MPLIC scheme is similar to the Piecewise-Linear Interface Calculation (PLIC), where each cell is split to match the volume fraction of the phase in that cell, but has the extra capabilities of splitting cells multiple times, when one split is insufficient [Greenshields (2020)].

4.5 Time discretisation scheme

As the time discretisation scheme, it is desirable to use a second order scheme to avoid a numerical dissipation of the turbulence. Only the first order accurate Euler Scheme or the second order accurate Crank-Nicolson scheme is available within the LES-VOF framework of the OpenFOAM version used in this study. These schemes are shown in Equation 4.6 and 4.7 respectively.

$$\frac{\partial}{\partial t}(\psi) = \frac{\psi - \psi^0}{\Delta t} \quad (4.6)$$

$$\frac{\partial}{\partial t}(\psi) = \frac{\psi - \psi^{00}}{2\Delta t} \quad (4.7)$$

ψ and ψ^0 represents the value at the current and previous time step respectively, while ψ^{00} represents the value at the time step before the previous.

When using the Crank-Nicolson scheme a coefficient between 0 and 1 needs to be specified. When a coefficient of 1 is specified the scheme is pure Crank-Nicolson, while specifying a coefficient of 0 makes the scheme pure Euler. If a coefficient between 0 and 1 is specified, the scheme is blended based on the chosen value.

In this project it is chosen to use the Crank Nicolson discretisation scheme with a coefficient of 0.9, as this generally ensures solution stability [Greenshields and Weller (2022)].

4.6 Simulations performed in this study

In this study three single-phase simulations are performed. These are performed on a coarse, medium and fine mesh to ensure that the results are independent of the mesh size and to validate the single-phase computational model. Five multi-phase simulations are performed with varying air volume fractions, to analyse the effect of the air volume fraction on the frictional resistance represented by the wall shear stress.

Chapter 5

Validation of single-phase model

Prior to performing the VOF simulations, single-phase simulations are performed to validate the LES single-phase computational model and to obtain a turbulent velocity profile to initialise the multi-phase simulations.

5.1 Parameters of interest

To obtain the space and time averaged velocity profiles, the velocity in each cell is averaged over each time interval of 0.01 s, which is the time it takes for the fluid to travel a distance of 50 mm, which is the length of the domain. This is done using Equation 5.1.

$$\langle \mathbf{u} \rangle = \frac{1}{t_1 - t_0} \int_{t_0}^{t_1} \mathbf{u}(x, y, z, t) dt \quad (5.1)$$

$\langle \mathbf{u} \rangle$ is time averaged velocity vector in each cell averaged over each passage through the domain. To obtain a single mean velocity profile in the wall normal direction for each mesh, $\langle \mathbf{u} \rangle$ is averaged in space by averaging over each x, z plane at each layer of cells in the wall normal direction. This process is described using Equation 5.2.

$$\langle \bar{\mathbf{u}} \rangle = \frac{1}{x_1 - x_0} \frac{1}{z_1 - z_0} \int_{x_0}^{x_1} \int_{z_0}^{z_1} \langle \mathbf{u} \rangle dx \quad (5.2)$$

5.2 Comparison of the meshes

In Figure 5.1 the space and time averaged velocity profiles for each mesh at the simulated time $t_{\text{sim}} = 0.4$ s, which corresponds to a downstream distance of 2 m. It is seen that the shape of the velocity profile converge towards the fine mesh, with a larger difference between the coarse and medium mesh, than between the medium and fine mesh.

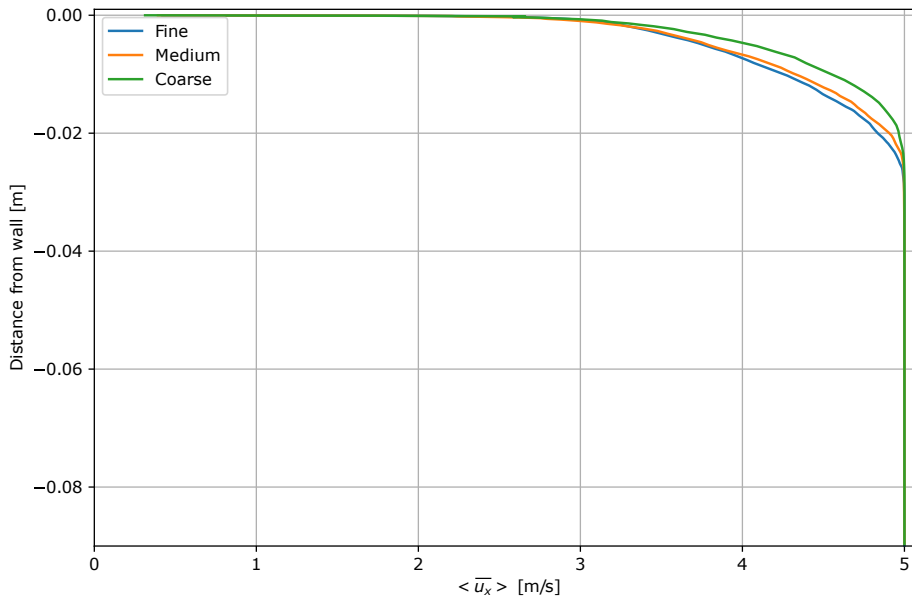


Figure 5.1: Space and time averaged velocity profiles for each mesh at $t_{\text{sim}} = 0.4$ s, which corresponds to a downstream distance of 2 m.

To validate the space and time averaged velocity profiles, they are compared with the the law of the wall which describes the relation between the dimensionless velocity and distance from the wall u^+ and y^+ in the turbulent boundary layer as described in Section 3.1. This comparison between the law of the wall and the different meshes is shown in Figure 5.2. The vertical dashed lines represent the different regions of the boundary layer. As seen in the figure all meshes follow the law of the wall in the viscous sublayer. In the overlap layer all meshes follow the tendency of the law of the wall. The coarse mesh overestimates u^+ , while the medium and fine meshes slightly underestimate u^+ .

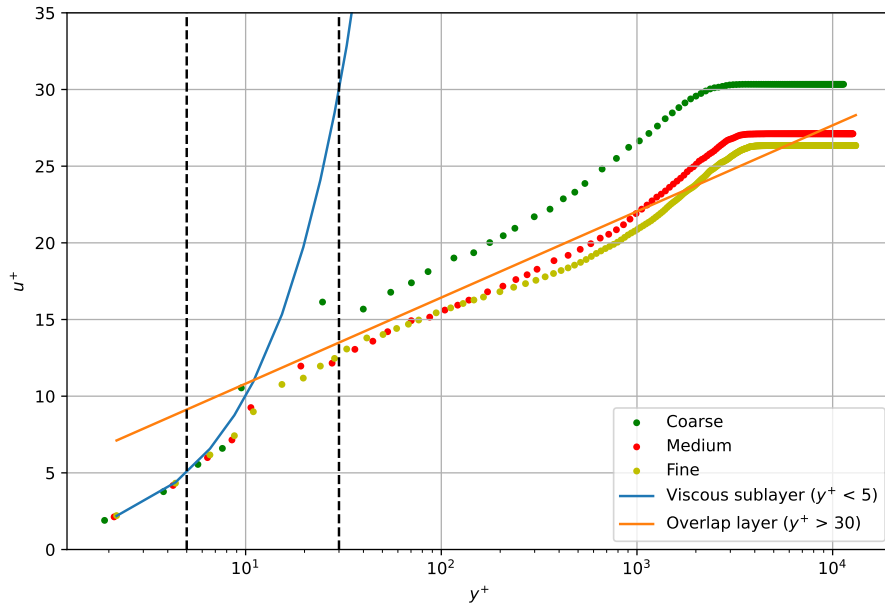


Figure 5.2: Law of the wall plotted against the dimensionless velocity u^+ as function of the dimensionless distance y^+ for the different meshes at $t_{\text{sim}} = 0.4$ s, which corresponds to a downstream distance of 2 m.

Furthermore it is seen that for all meshes the relation between u^+ and y^+ plateaus at approximately the same y^+ distance away from the wall. This happens at the y^+ value corresponding to the turbulent boundary layer thickness δ , where the velocity is equal to the free stream velocity. To compare with the theory, the theoretical boundary layer thickness using Equation 3.2 is 0.031 m, whereas the boundary layer thickness in the simulations is 0.029, 0.033 and 0.032 m for the coarse, medium and fine mesh respectively.

For these reasons, the single-phase computational model and the turbulent velocity profiles obtained using this model is validated against the theory. As the results from the medium and fine mesh both follow the law of the wall in a similar way, it is chosen to use the medium mesh for the multi-phase simulations.

Chapter 6

Results

As mentioned in Section 5.2 the results from the medium mesh agrees just as well with the law of the wall as the fine mesh, which is why it is chosen to use the medium mesh for the multi-phase simulations.

The cells in block 5, which are the coarsest cells, however, have a size of $0.96 \times 0.48 \times 0.96$ mm in the x , y and z direction respectively, and as the air bubbles have an initial diameter of $d = 2$ mm, it is chosen to extend block 4 with cells of the size $0.48 \times 0.24 \times 0.48$ mm in the wall normal direction such that it covers half of the domain, in order to resolve the interface of the air bubbles. This increases the number of cells in the mesh from 5,105,251 to 9,128,146, but the increase in computational demand is expected to be worthwhile to achieve a better resolved interface of the air bubbles.

To compare the results with the validated single-phase computational model, a single-phase simulation is performed on the multi-phase mesh. This is done in the same way as with the multi-phase simulations, by initialising the simulation with the single-phase turbulent velocity profile obtained with the single-phase simulations.

6.1 Air bubble behaviour

To analyse the behaviour of the air bubbles, their locations are visualised at 4 simulated times $t_{\text{sim}} = 0.01, 0.1, 0.2, 0.4$ s, as seen for case 5 ($\varphi = 50\%$) in Figure 6.1, 6.2, 6.3 and 6.4. At $t_{\text{sim}} = 0.01$ s in Figure 6.1 the bubbles near the wall within the turbulent boundary layer coalesce in all directions because of the turbulence in the flow. The location of the bubbles further away from the wall outside the boundary layer is only slightly different from their initialisation, as they only coalesce vertically due to the buoyancy. From $t_{\text{sim}} = 0.1 - 0.4$ s the air coalesce to form an air

layer near the wall, whereas further away from the wall, individual air bubbles are seen. Similar air bubble behaviour is seen for the other cases with lower air volume fractions as seen in Appendix B.1.

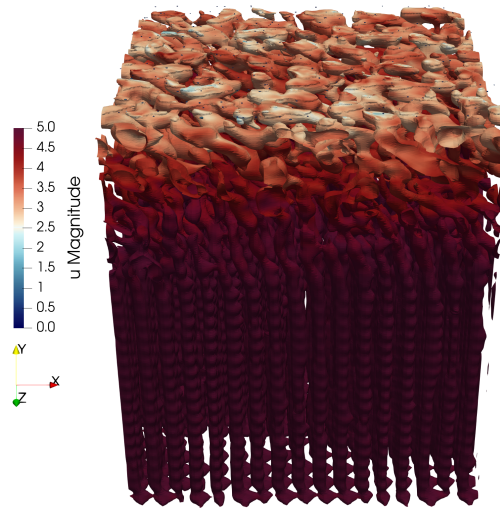


Figure 6.1: Contour plot of the air at $t_{\text{sim}} = 0.01$ s in case 5 ($\varphi = 50\%$), coloured with the absolute velocity $|u|$.

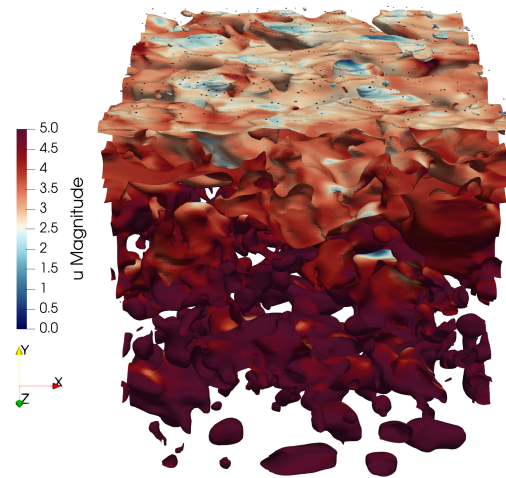


Figure 6.2: Contour plot of the air at $t_{\text{sim}} = 0.1$ s in case 5 ($\varphi = 50\%$), coloured with the absolute velocity $|\mathbf{u}|$.

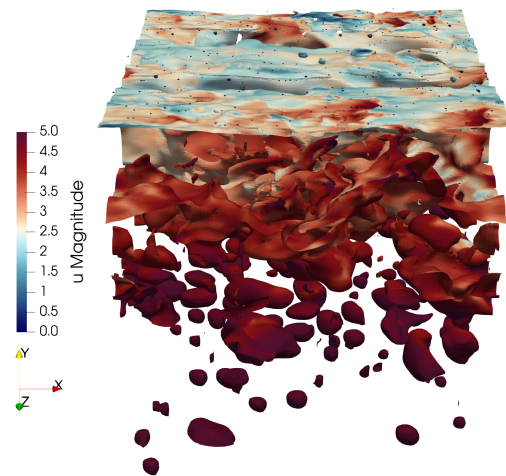


Figure 6.3: Contour plot of the air at $t_{\text{sim}} = 0.2$ s in case 5 ($\varphi = 50\%$), coloured with the absolute velocity $|\mathbf{u}|$.

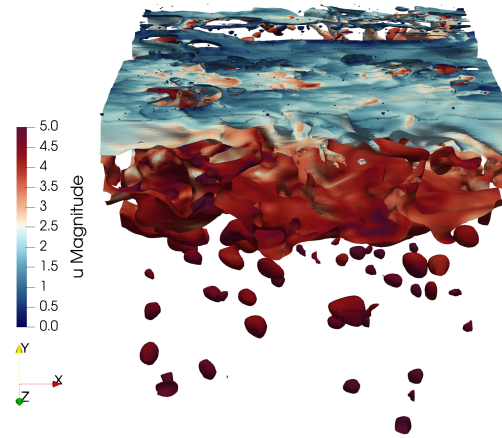


Figure 6.4: Contour plot of the air at $t_{\text{sim}} = 0.4$ s in case 5 ($\varphi = 50\%$), coloured with the absolute velocity $|\mathbf{u}|$.

It is suspected that the individual air bubbles originate from the turbulence in the flow causing air bubbles to split up from the air layer. To test this hypothesis the vorticity, which is the curl of the velocity, described by Equation 6.1 is calculated for the flow.

$$\boldsymbol{\omega} = \nabla \times \mathbf{u} \quad (6.1)$$

In Figure 6.5 the magnitude of the vorticity $|\boldsymbol{\omega}|$ is visualised for case 5 at $t_{\text{sim}} = 0.4$ s on an x, y plane parallel to the flow in the middle of the domain at $z = 25$ mm. The black contour represents the interface of the air bubbles. It appears as though the air bubbles do in fact get split up from the layer of air, by the vorticity in the flow, as the bubbles are shaped by the areas of high vorticity. Similar findings are seen for the other cases as shown in Appendix B.2.

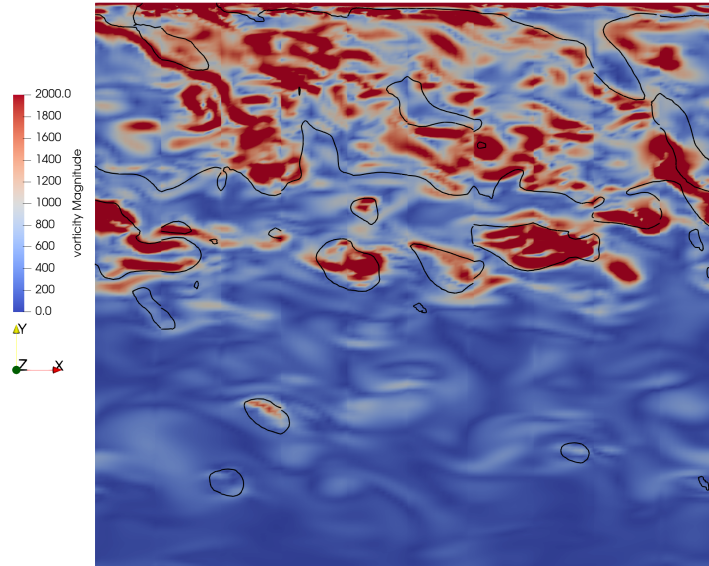


Figure 6.5: Magnitude of the vorticity $|\omega|$ and contour of the air bubbles for case 5 at $t_{\text{sim}} = 0.4$ s.

6.2 Wall shear stress

As the solver used in the LES-VOF framework of OpenFOAM is incompressible, the effective density of the fluids ρ_ϕ is not accounted for in calculation of the wall shear stress τ_w . The source code of the calculation of τ_w is therefore modified by multiplying with ρ_ϕ as described in Equation 6.2.

$$\tau_{w,\phi} = \tau_w \rho_\phi \quad (6.2)$$

The magnitude of the average wall shear stress $|\overline{\tau_{w,\phi}}|$ is determined by calculating the magnitude of the area averaged wall shear stress on the surface of the wall each write time of 0.01 s in the simulations.

In Figure 6.6 $|\overline{\tau_{w,\phi}}|$ is shown as function of the simulated time for the single-phase simulation compared against the theoretical values, which are determined using Equation 3.16, where the skin friction coefficient is determined using the Schultz-Grunov relation shown in Equation 6.3 [Schlichting (1979)].

$$cf = 0.37(\log_{10}(Re_x))^{-2.584} \quad (6.3)$$

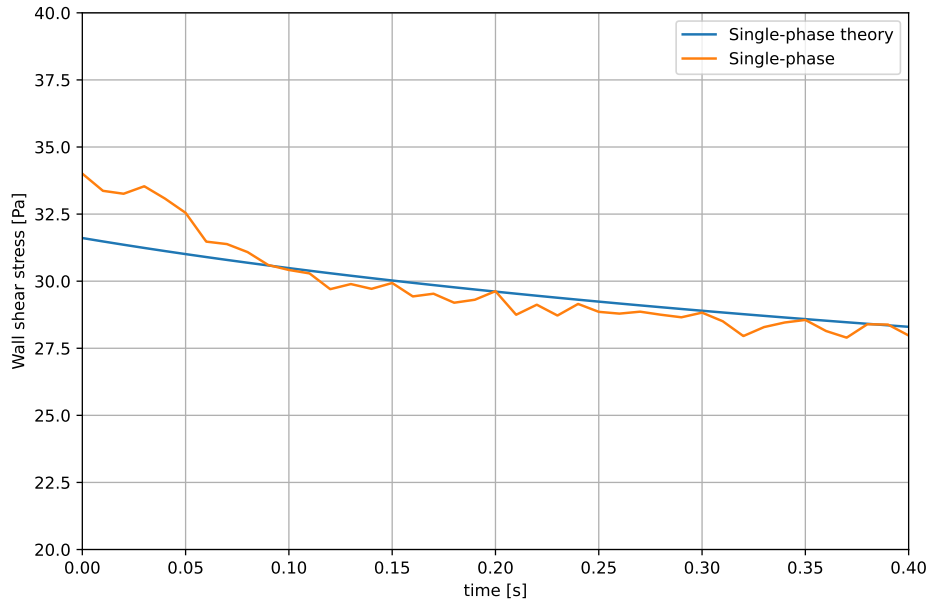


Figure 6.6: The absolute wall shear stress $|\bar{\tau}_{w,\varphi}|$ as function of the simulated time t_{sim} for the single-phase simulation compared with theory.

As seen in the figure $|\bar{\tau}_{w,\varphi}|$ from the single-phase simulation is in good agreement with the theory. This was expected as the single-phase computational model was validated against the law of the wall in Chapter 5.

For the results from the multi-phase simulations, seen in Figure 6.7, the values of $|\bar{\tau}_{w,\varphi}|$ are normalised with respect to the single-phase values. The results from the multi-phase simulations follow the same general trend as the single-phase results, namely that $|\bar{\tau}_{w,\varphi}|$ is decreasing as function of the simulated time. In all the multi-phase simulations $|\bar{\tau}_{w,\varphi}|$ is lower than in the single-phase simulation. For case 1 a reduction of 20 - 40% is seen while for the other cases, the reduction is 40 - 60% compared to single-phase values. The largest decrease in $|\bar{\tau}_{w,\varphi}|$ between the cases is seen between case 1 and 2, where a significant decrease in $|\bar{\tau}_{w,\varphi}|$ as function of φ is seen. Between the other cases, this relation is not obvious, as the results are fluctuating.

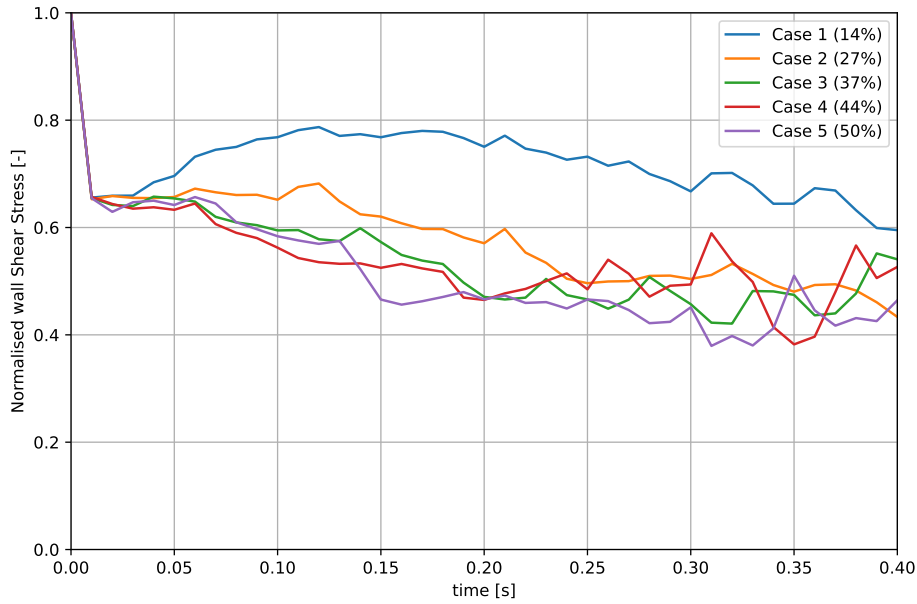


Figure 6.7: The normalised absolute wall shear stress $|\bar{\tau}_{w,\varphi}|$ as function of the simulated time t_{sim} for the multi-phase cases.

A plausible explanation of the fluctuations, is that the area of the wall covered with air varies between a write interval of 0.01 s. If the write interval was shorter, these fluctuations could be analysed in detail, and the fluctuations would perhaps not be as drastic as seen in the figure.

To determine the cause of the fluctuations, the increase in $|\bar{\tau}_{w,\varphi}|$ with case 4 at $0.30 \text{ s} < t_{\text{sim}} < 0.31 \text{ s}$ is analysed by comparing the wall shear stress in detail visually. In Figure 6.8 and 6.9 the magnitude of the wall shear stress $|\tau_w|$ on the surface of the wall is shown as well as a contour plot of $\alpha = 0.5$ to visualise the interface between air and water, for case 4 at $t_{\text{sim}} = 0.30 \text{ s}$ and $t_{\text{sim}} = 0.31 \text{ s}$ respectively. From the figures it is seen that the higher $|\bar{\tau}_{w,\varphi}|$ at $t_{\text{sim}} = 0.31 \text{ s}$ is composed of a smaller area of low wall shear stress due to the presence of air as well as a larger area of high wall shear stress.

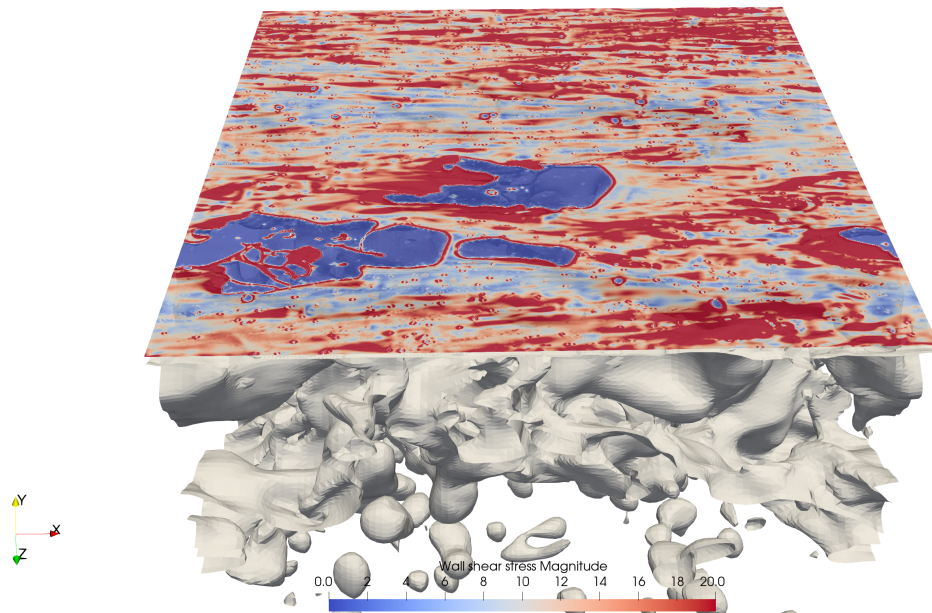


Figure 6.8: Magnitude of the wall shear stress $|\tau_{w,\phi}|$ on the surface of the wall and contour plot of $\alpha = 0.5$ at $t_{\text{sim}} = 0.30$ s.

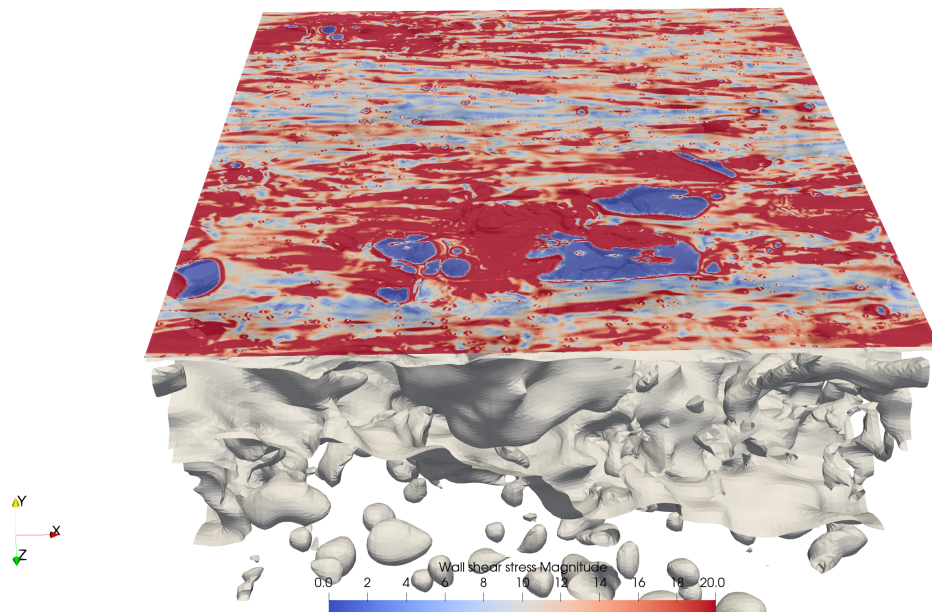


Figure 6.9: Magnitude of the wall shear stress $|\tau_{w,\phi}|$ on the surface of the wall and contour plot of $\alpha = 0.5$ at $t_{\text{sim}} = 0.31$ s.

To determine if the air layer drag reduction (ALDR) regime, in which the highest drag reduction is achievable according to the study by Elbing et al. (2008), is obtained in the simulations, the contour of the air interface is visualised seen from the top. In Figure 6.10 this is shown for case 5 at $t_{\text{sim}} = 0.31\text{s}$, where the highest drag reduction in terms of $|\bar{\tau}_{w,\varphi}|$ is achieved throughout the simulations, as seen in Figure 6.7. As seen in the Figure, the air is not covering the entire surface of the wall as a continuous air layer but appears to be unstable and breaking up, which resembles the characteristics of the transition regime of drag reduction. This suggests that the ALDR regime is not achieved in the simulations performed in this study.

To further investigate if the the ALDR regime is obtainable with the flow conditions used in this study, the simulated time could be extended to determine if a simulated time of 0.4 s is inadequate to achieve a stable air layer. In addition the structures of the air seen in the simulations extends all across the periodic domain in the x and z direction, which suggests that the structures are larger than the size of the domain. This could be analysed by extending the domain.

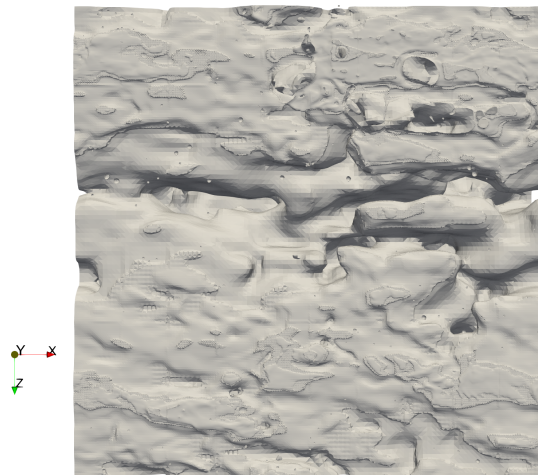


Figure 6.10: Contour of the air interface at the point of highest drag reduction throughout the simulations.

Chapter 7

Conclusion

In this study a series of multi-phase Large Eddy Simulations with the Volume Of Fluid approach have been made to analyse the use of air lubrication to reduce the drag on a ship by injecting air bubbles underneath the hull. The Volume Of Fluid approach was chosen, as oppose to other less computationally demanding multi-phase methods, as it makes it possible to resolve the interface between the air and the water of each air bubble, which allows to analyse the dynamics of the air bubbles and the effect of those on the drag reduction. As the Volume of Fluid approach is computationally demanding, it is not possible to analyse the effect of air lubrication across an entire hull of a ship. Because of this a smaller domain of the size 50 x 180 x 50 mm was used with periodic boundary conditions with the surface of the hull represented as a flat plate. The velocity of the flow in the simulations was 5 m/s, and the simulated time was limited to 0.4 s, corresponding to a streamwise distance of 2 m.

A single-phase computational model was developed to obtain a turbulent velocity profile, which was used to initialise the flow in the multi-phase simulations. To ensure that the results of the single-phase simulation were independent of the mesh size, a grid convergence study was made. Furthermore the model was validated against theory, by comparing the turbulent boundary layer with the law of the wall.

Five multi-phase simulations were performed, where the air volume fraction was varied from 14 - 50% to analyse the effect of the air volume fraction on the drag reduction. At the start of the simulations, bubbles with a diameter $d = 2$ mm were inserted uniformly inside and outside of the turbulent boundary layer, to analyse the air bubble behaviour inside as well as outside of the turbulent boundary layer. Throughout the simulations two types of air bubble behaviour were seen; a coalescence of bubbles forming an air layer in the boundary layer near the wall and a splitting up of bubbles further away from the wall, where the latter was deemed to

be caused by the vorticity in the flow.

The drag reduction with the use of air lubrication was analysed by comparing the wall shear stress for a case without air bubbles and the five cases with varying air volume fractions. A reduction in wall shear stress and thereby a reduction in drag was seen in the multi-phase simulations compared to the single-phase simulation. The wall shear stress decreased with 20 - 40% in case 1 with an air volume fraction of 14% compared to the wall shear stress in the single-phase simulation. For the other cases with air volume fractions of 27 - 50% the reduction in wall shear stress fluctuated from 40 - 60%. Analysing the structure of the air in the simulations it was found that the regime of highest achievable drag reduction with air lubrication, Air Layer Drag Reduction, was not obtained in the simulations. By further increasing the air volume fraction, the Air Layer Drag Reduction regime could possibly be obtained, thereby increasing the drag reduction.

7.1 Future work

The use of Adaptive Mesh Refinement (AMR) could be a promising area of interest when analysing the effects of air lubrication with the VOF approach, as this could improve the resolved interface of the air bubbles.

It was not chosen to use AMR in this study as it was found to increase the computational demand by approximately a factor 100. In Figure 7.1 the use of AMR is seen, where the mesh is refined around the bubbles to achieve a sharper interface. No significant improvement of the resolved interface is seen, as to why the use of AMR was not justified in this study. AMR is still expected to be a useful tool, as it allows to use a coarser initial mesh, and with a tweaking of the refinement properties, a decrease in computational demand should be obtained.

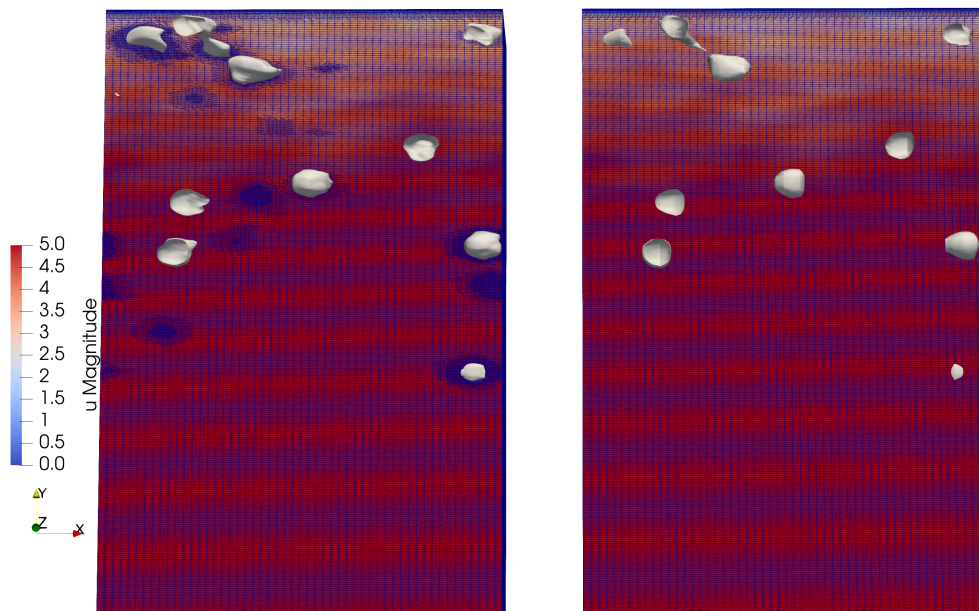


Figure 7.1: Comparison of the mesh and resolved interface with the use of AMR (left figure) and without (right figure).

When resolving the interface of an air layer the improvement with the use of AMR is more significant as seen in Figure 7.2, hence it is a promising tool for the VOF approach of analysing the effect of air lubrication, if a reduction in computational demand is achieved.

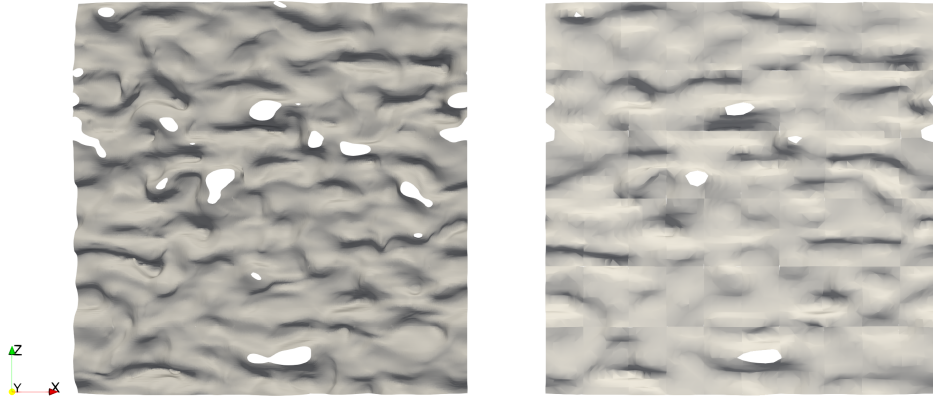


Figure 7.2: Comparison of the resolved interface of an air layer seen from the top with the use of AMR (left figure) and without (right figure).

References

- American Bureau of Shipping (2019). *Air Lubrication Technology*. Tech. rep.
- Ansys and Inc (2009). *Chapter 16. Multiphase Flows*. Tech. rep.
- Cengel, Yunus A., John M. Cimbala, and Robert H. Turner (2017). *Fundamentals of Thermal-Fluid Sciences*. McGrawHill. ISBN: 9789814720953.
- Elbing, Brian R. et al. (2008). "Bubble-induced skin-friction drag reduction and the abrupt transition to air-layer drag reduction". In: *Journal of Fluid Mechanics* 612, pp. 201–236. ISSN: 00221120. DOI: 10.1017/S0022112008003029.
- EU (Dec. 2020). *SUBMISSION BY GERMANY AND THE EUROPEAN COMMISSION ON BEHALF OF THE EUROPEAN UNION AND ITS MEMBER STATES*. Tech. rep. Berlin: EU. URL: <https://unfccc.int/process/the-paris-agreement/long-term-strategies>.
- Fenhann, J.V (2017). "CO2 Emissions from International Shipping". In: *UNEP DTU Partnership Working Paper Series 4*.
- Greenshields, Chris (2020). *Interface Capturing in OpenFOAM | CFD Direct*. URL: <https://cfd.direct/openfoam/free-software/multiphase-interface-capturing/>.
- Greenshields, Christopher. and Henry. Weller (2022). *Notes on computational fluid dynamics : general principles*. CFD Direct Ltd. ISBN: 978-1-3999-2078-0.
- IMO (2020). *Fourth IMO GHG Study 2020 Full Report*. Tech. rep.
- Jha, Narsing K., Anubhav Bhatt, and Raghuraman N. Govardhan (Aug. 2019). "Effect of bubble distribution on wall drag in turbulent channel flow". In: *Experiments in Fluids* 60.8. ISSN: 14321114. DOI: 10.1007/s00348-019-2773-7.
- Kato, Hiroharu et al. (1999). *Effect of microbubbles on the structure of turbulence in a turbulent boundary layer*. Tech. rep., pp. 155–162.
- Kawamura, T. et al. (2002). "Effect of bubble size on the microbubble drag reduction of a turbulent boundary layer". In: *The proceedings of the JSME annual meeting 2002.7.0*, pp. 55–56. DOI: 10.1299/JSMEMECJ0.2002.7.0{_}55.
- Legner, Hartmut H. (1984). "A simple model for gas bubble drag reduction". In: *Physics of Fluids* 27.12, pp. 2788–2790. ISSN: 10706631. DOI: 10.1063/1.864592.
- Mäkiharju, Simo A., Marc Perlin, and Steven L. Ceccio (Dec. 2012). "On the energy economics of air lubrication drag reduction". In: *International Journal of Naval*

- Architecture and Ocean Engineering* 4.4, pp. 412–422. ISSN: 20926782. DOI: 10.2478/IJNAOE-2013-0107. URL: <http://dx.doi.org/10.2478/>.
- Merkle, C. L. et al. (1989). “Microbubble Drag Reduction”. In: pp. 291–335. DOI: 10.1007/978-3-642-83831-6_{_}6. URL: https://link.springer.com/chapter/10.1007/978-3-642-83831-6_6.
- Nicoud, F and F Ducros (1999). “Subgrid-Scale Stress Modelling Based on the Square of the Velocity Gradient Tensor”. In: *Flow, Turbulence and Combustion* 62, pp. 183–200.
- Schlichting, H. (1979). *Boundary layer theory: Seventh edition*. McGraw-Hill Book Co. ISBN: 0070553343. DOI: 10.1115/1.3240614.
- Schlichting, Hermann and Klaus Gersten (Oct. 2016). *Boundary-Layer Theory*. Springer Berlin Heidelberg, pp. 1–799. ISBN: 9783662529195. DOI: 10.1007/978-3-662-52919-5.
- Shen, Xiaochun, Steven L. Ceccio, and Marc Perlin (Sept. 2006). “Influence of bubble size on micro-bubble drag reduction”. In: *Experiments in Fluids* 41.3, pp. 415–424. ISSN: 07234864. DOI: 10.1007/s00348-006-0169-y.
- Skudarnov, P. V. and C. X. Lin (June 2006). “Drag reduction by gas injection into turbulent boundary layer: Density ratio effect”. In: *International Journal of Heat and Fluid Flow* 27.3, pp. 436–444. ISSN: 0142727X. DOI: 10.1016/j.ijheatfluidflow.2005.12.002.
- Takahashi, Takahito et al. (2001). *Mechanisms and Scale Effects of Skin Friction Reduction by Microbubbles*. Tech. rep. Ship Research Institute.
- Tripathi, Manoj Kumar, Kirti Chandra Sahu, and Rama Govindarajan (Feb. 2015). “Dynamics of an initially spherical bubble rising in quiescent liquid”. In: *Nature Communications* 6. ISSN: 20411723. DOI: 10.1038/ncomms7268.
- UNFCCC (2015). *ADOPTION OF THE PARIS AGREEMENT - Paris Agreement text English*. Tech. rep.
- Versteeg, H and W Malalasekera (2007). *Introduction to Computational Fluid Dynamics*.
- Wang, Tongsheng et al. (July 2020). “Large eddy simulation of microbubble drag reduction in fully developed turbulent boundary layers”. In: *Journal of Marine Science and Engineering* 8.7. ISSN: 20771312. DOI: 10.3390/JMSE8070524.

Appendix A

Equations

A.1 Equations used to determine the height of the cells closest to the wall

The following set of equations are used to determine the height of the first layer of cells closest to the wall, based on the cells being placed at $y^+ = 1$.

The wall shear stress is calculated using Equation A.1, in which the skin friction coefficient is determined using Equation 6.3.

$$\tau_w = \frac{1}{2} cf \rho u_\infty^2 \quad (\text{A.1})$$

The friction velocity is calculated using A.2

$$u_\tau = \sqrt{\frac{\tau_w}{\rho}} \quad (\text{A.2})$$

The distance from the wall to the centre of the cells closest to the wall is determined using Equation A.3, where $y^+ = 1$

$$\Delta y_{\text{centre}} = \frac{y^+ \nu}{u_\tau} \quad (\text{A.3})$$

Finally the height of the first layer of cells closest to the wall is determined using Equation A.4.

$$\Delta y = 2 \cdot \Delta y_{\text{centre}} \quad (\text{A.4})$$

Appendix B

Results

B.1 Air bubble behaviour

B.1.1 Case 1 ($\varphi = 14\%$)

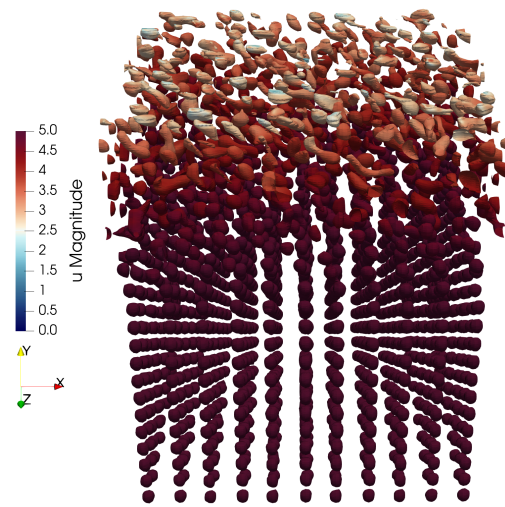


Figure B.1: Contour plot of the air at $t_{\text{sim}} = 0.01$ s in case 1 ($\varphi = 14\%$), coloured with the absolute velocity $|u|$.

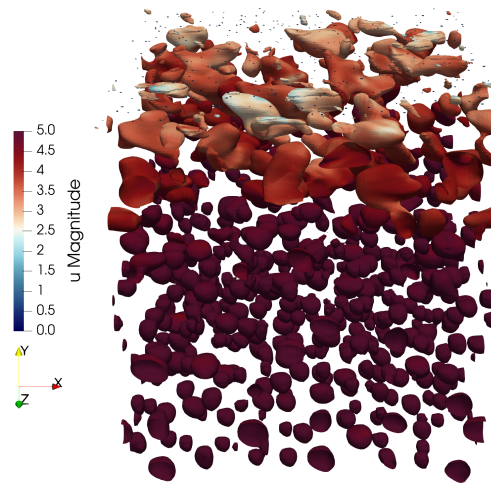


Figure B.2: Contour plot of the air at $t_{\text{sim}} = 0.1$ s in case 1 ($\varphi = 14\%$), coloured with the absolute velocity $|\mathbf{u}|$.

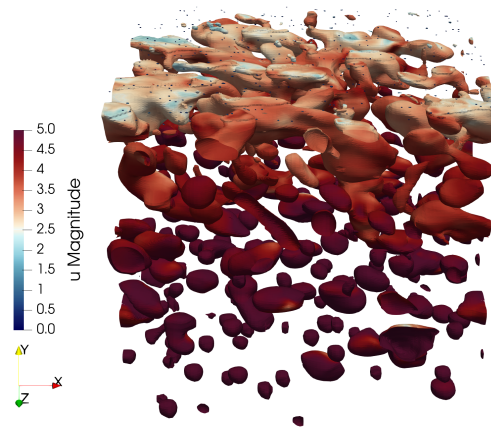


Figure B.3: Contour plot of the air at $t_{\text{sim}} = 0.2$ s in case 1 ($\varphi = 14\%$), coloured with the absolute velocity $|\mathbf{u}|$.

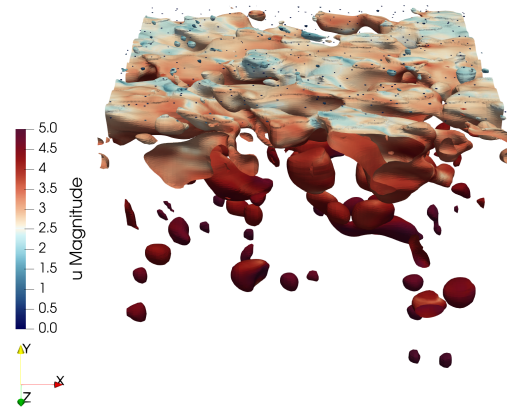


Figure B.4: Contour plot of the air at $t_{\text{sim}} = 0.4$ s in case 1 ($\varphi = 14\%$), coloured with the absolute velocity $|\mathbf{u}|$.

B.1.2 Case 2 ($\varphi = 27\%$)

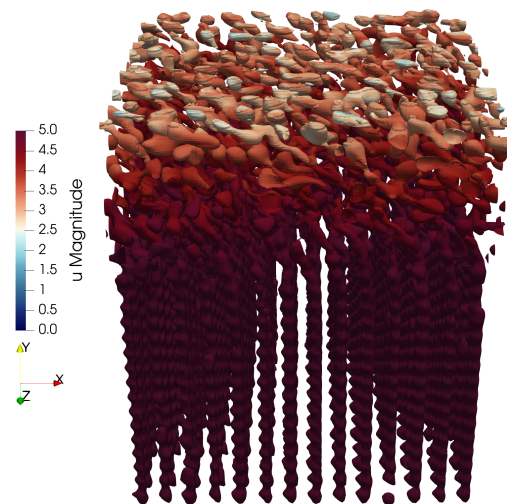


Figure B.5: Contour plot of the air at $t_{\text{sim}} = 0.01$ s in case 2 ($\varphi = 27\%$), coloured with the absolute velocity $|\mathbf{u}|$.

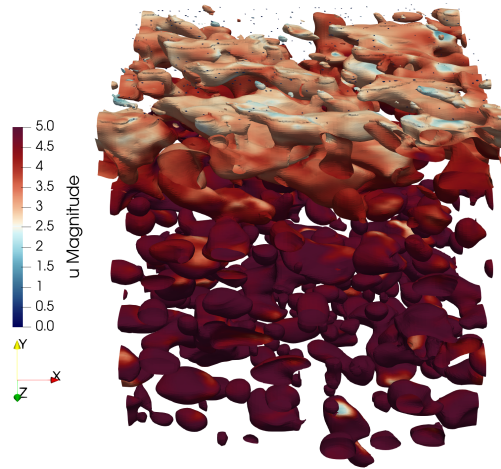


Figure B.6: Contour plot of the air at $t_{\text{sim}} = 0.1$ s in case 2 ($\varphi = 27\%$), coloured with the absolute velocity $|\mathbf{u}|$.

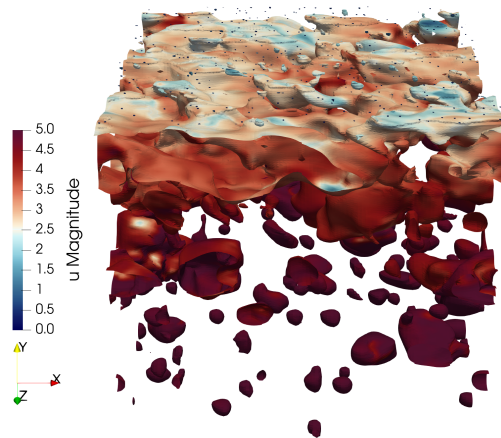


Figure B.7: Contour plot of the air at $t_{\text{sim}} = 0.2$ s in case 2 ($\varphi = 27\%$), coloured with the absolute velocity $|\mathbf{u}|$.

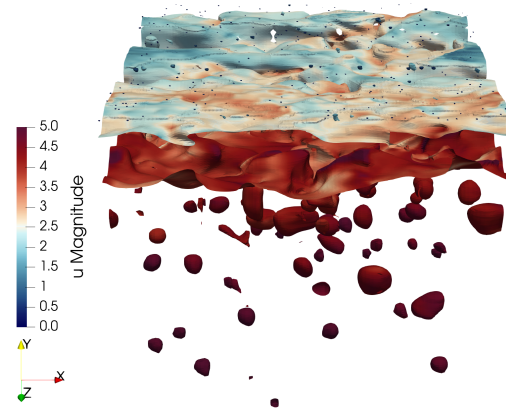


Figure B.8: Contour plot of the air at $t_{\text{sim}} = 0.4$ s in case 2 ($\varphi = 27\%$), coloured with the absolute velocity $|\mathbf{u}|$.

B.1.3 Case 3 ($\varphi = 37\%$)

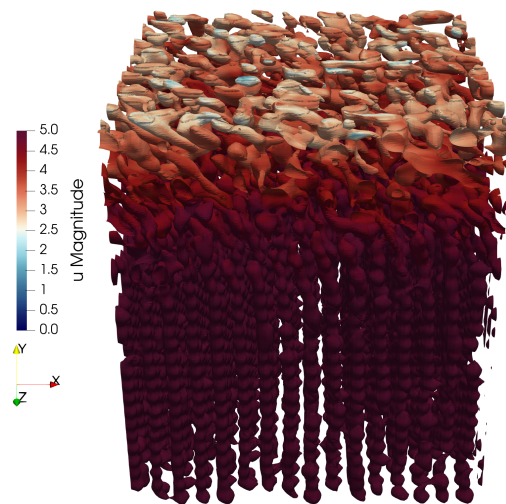


Figure B.9: Contour plot of the air at $t_{\text{sim}} = 0.01$ s in case 3 ($\varphi = 37\%$), coloured with the absolute velocity $|\mathbf{u}|$.

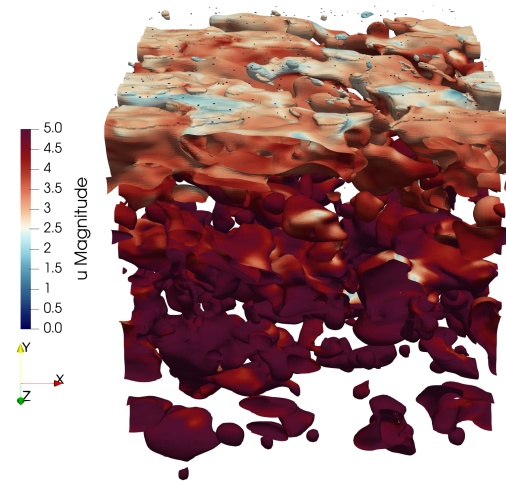


Figure B.10: Contour plot of the air at $t_{\text{sim}} = 0.1$ s in case 3 ($\varphi = 37\%$), coloured with the absolute velocity $|\mathbf{u}|$.

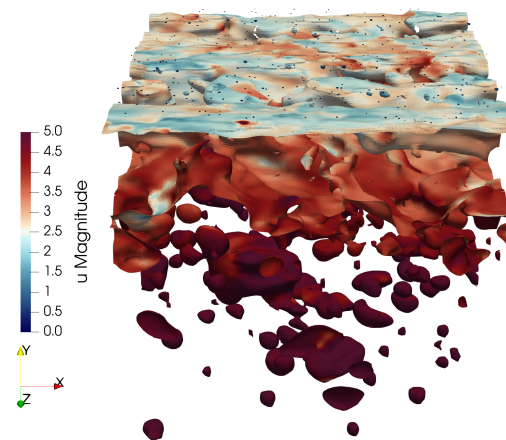


Figure B.11: Contour plot of the air at $t_{\text{sim}} = 0.2$ s in case 3 ($\varphi = 37\%$), coloured with the absolute velocity $|\mathbf{u}|$.

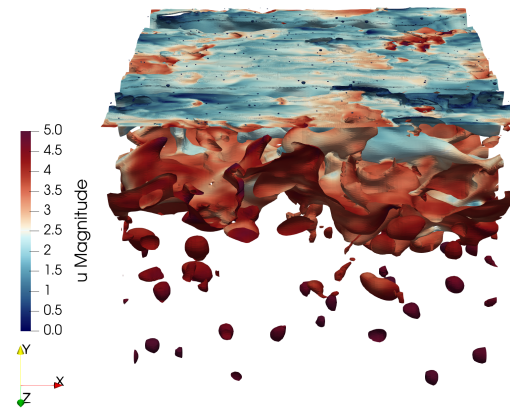


Figure B.12: Contour plot of the air at $t_{\text{sim}} = 0.4$ s in case 3 ($\varphi = 37\%$), coloured with the absolute velocity $|\mathbf{u}|$.

B.1.4 Case 4 ($\varphi = 44\%$)

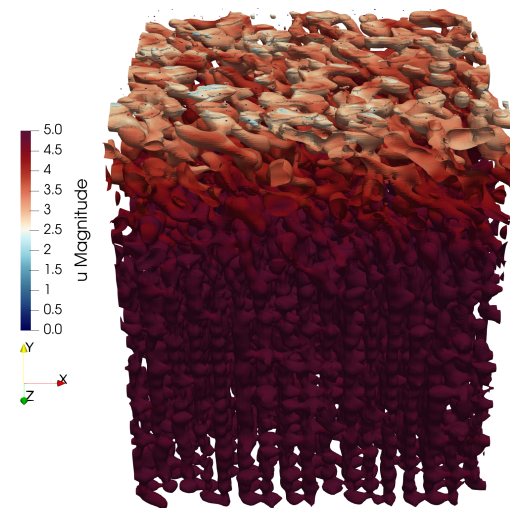


Figure B.13: Contour plot of the air at $t_{\text{sim}} = 0.01$ s in case 4 ($\varphi = 44\%$), coloured with the absolute velocity $|\mathbf{u}|$.

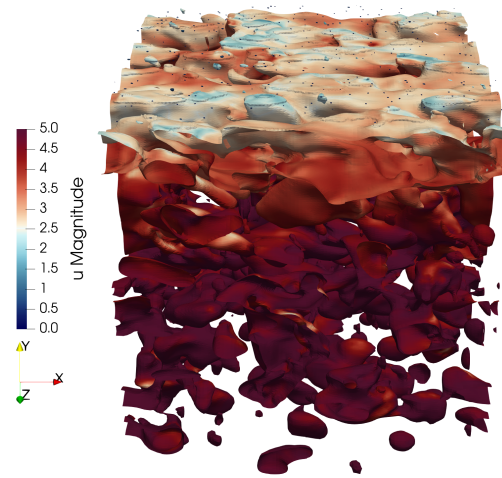


Figure B.14: Contour plot of the air at $t_{\text{sim}} = 0.1$ s in case 4 ($\varphi = 44\%$), coloured with the absolute velocity $|\mathbf{u}|$.

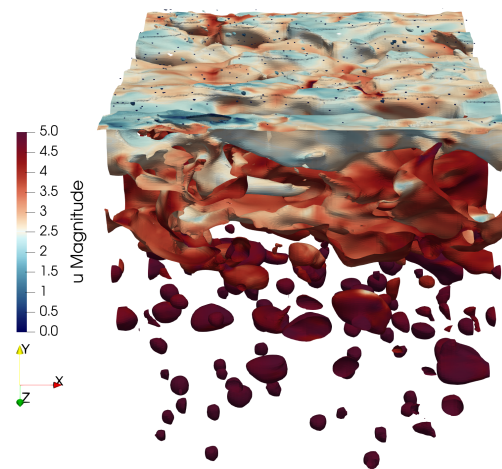


Figure B.15: Contour plot of the air at $t_{\text{sim}} = 0.2$ s in case 4 ($\varphi = 44\%$), coloured with the absolute velocity $|\mathbf{u}|$.

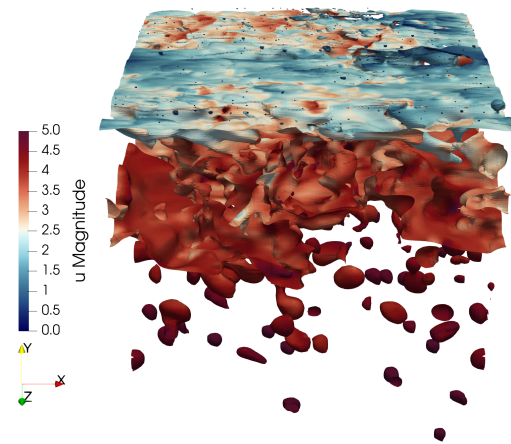


Figure B.16: Contour plot of the air at $t_{\text{sim}} = 0.4$ s in case 4 ($\varphi = 44\%$), coloured with the absolute velocity $|\mathbf{u}|$.

B.2 Vorticity

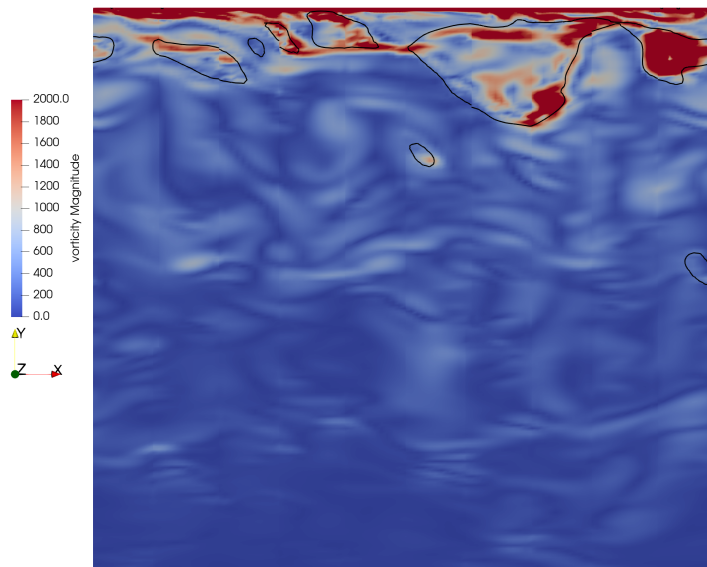


Figure B.17: Magnitude of the vorticity $|\omega|$ and contour of the air bubbles for case 1 at $t_{\text{sim}} = 0.4$ s.

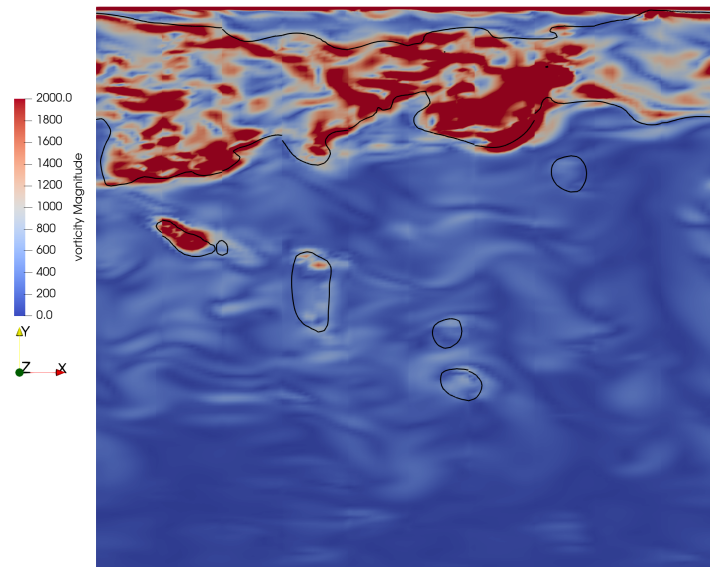


Figure B.18: Magnitude of the vorticity $|\omega|$ and contour of the air bubbles for case 2 at $t_{\text{sim}} = 0.4$ s.

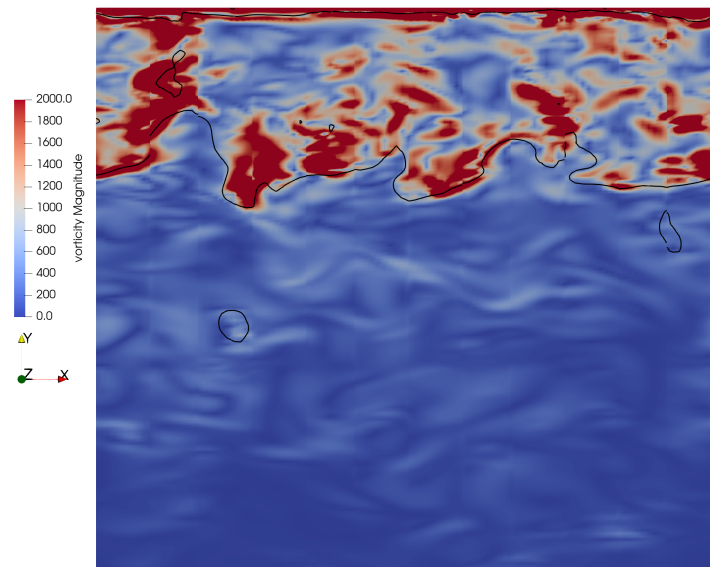


Figure B.19: Magnitude of the vorticity $|\omega|$ and contour of the air bubbles for case 3 at $t_{\text{sim}} = 0.4$ s.

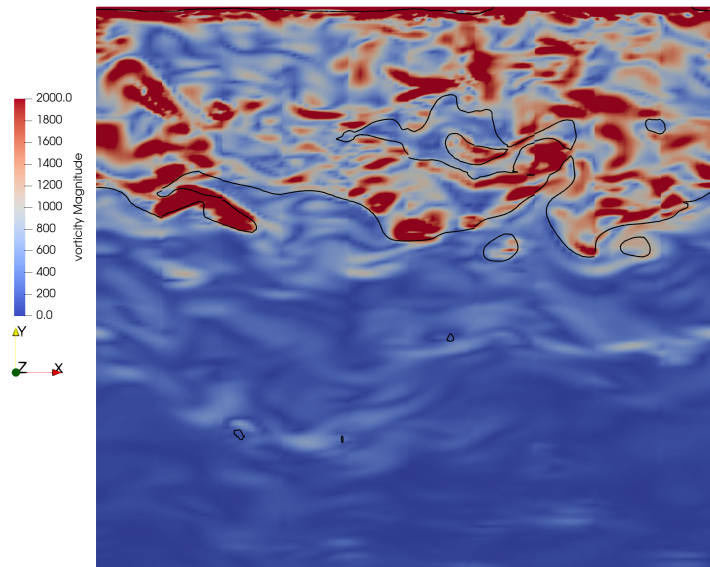


Figure B.20: Magnitude of the vorticity $|\omega|$ and contour of the air bubbles for case 4 at $t_{\text{sim}} = 0.4$ s.